

The strain-dependent spatial evolution of garnet in a high-pressure ductile shear zone from the Western Gneiss Region (Norway): a synchrotron X-ray microtomography study

Journal:	<i>Journal of Metamorphic Geology</i>
Manuscript ID	JMG-16-0051.R3
Manuscript Type:	Original Article
Date Submitted by the Author:	n/a
Complete List of Authors:	Macente, Alice; University of Edinburgh School of GeoSciences, School of Geosciences Füsseis, Florian; University of Edinburgh School of GeoSciences, School of Geosciences Menegon, Luca; Plymouth University, School of Geography, Earth and Environmental Sciences Xiao, Xianghui; Argonne National Laboratory, X-ray Science Division John, Timm; Freie Universität Berlin Institut für Geologische Wissenschaften, Institut für Geologische Wissenschaften
Keywords:	high-pressure shear zone, garnet, Western Gneiss Region, strain localisation, Synchrotron X-ray microtomography

The strain-dependent spatial evolution of garnet in a high-pressure ductile shear zone from the Western Gneiss Region (Norway): a synchrotron X-ray microtomography study

A. Macente^{1*}, F. Fousseis, L. Menegon², X. Xianghui³, T. John⁴

¹ School of Geosciences, The King's Building, James Hutton Road, Edinburgh, EH9 3FE

² School of Geography, Earth and Environmental Sciences (Faculty of Science and Engineering), Fitzroy, Drake Circus, Plymouth, Devon, PL4 8AA

³ Argonne National Laboratory, 9700 S. Cass Ave, Building 431-B003

⁴ Institut für Geologische Wissenschaften, Freie Universität Berlin, Malteserstr. 74-100, 12249 Berlin

* Corresponding author's e-mail:

alice.macente@ed.ac.uk, alice.macente@gmail.com

Short title: Strain-dependent evolution of garnet

ABSTRACT

Reaction and deformation microfabrics provide key information to understand the thermodynamic and kinetic controls of tectono-metamorphic processes, however they are usually analysed in two dimensions, omitting important information regarding the third spatial dimension. We applied synchrotron-based X-ray microtomography to document the evolution of a pristine olivine gabbro into a deformed omphacite-garnet eclogite in four dimensions, where the 4th dimension is represented by the degree of strain. In the investigated samples, which cover a strain gradient into a shear zone from the Western Gneiss Region (Norway), we focused on the spatial transformation of garnet coronas into elongated clusters of garnets with increasing strain. Our microtomographic data allowed quantification of garnet volume, shape and spatial arrangement evolution with increasing strain. We combined microtomographic observations with light microscope- and backscatter electron images as well as electron microprobe- (EMPA) and electron backscatter diffraction (EBSD) analysis to correlate mineral composition and orientation data with the X-ray absorption signal of the same mineral grains.

With increasing deformation, the garnet volume almost triples. In the low strain domain, garnets form a well interconnected large garnet aggregate that develops throughout the entire

sample. We also observed that garnet coronas in the gabbros never completely encapsulate olivine grains. In the most highly deformed eclogites, the oblate shapes of garnet clusters reflect a deformational origin of the microfabrics. We interpret the aligned garnet aggregates to direct synkinematic fluid flow and consequently influence the transport of dissolved chemical components. EBSD analyses reveal that garnet show a near-random crystal preferred orientation that testifies no evidence for crystal plasticity. There is, however evidence for minor fracturing, neo-nucleation and overgrowth. Microprobe chemical analysis revealed that garnet compositions progressively equilibrate to eclogite facies, becoming more almandine-rich. We interpret these observations as pointing to a mechanical disintegration of the garnet coronas during strain localisation, and their rearrangement into individual garnet clusters through a combination of garnet coalescence and overgrowth while the rock was deforming.

Key words:

Synchrotron X-ray microtomography; garnet; high-pressure shear zone; Western Gneiss Region; strain localisation;

INTRODUCTION

Synkinematic reaction microfabrics carry important information on the kinetics, timing, and mechanics of tectono-metamorphic processes. The spatial arrangement of reaction products reflects directions and magnitudes of mass and element transport. An assessment of the geometry of reaction microfabrics is therefore a critical component in reconstructing the tectono-metamorphic evolution of a rock. Despite being routinely interpreted in metamorphic and structural studies, reaction and deformation microfabrics are usually described in two dimensions, which could lead to incorrect petrographic and structural interpretations. In this study, we use garnet to explore the significance of a 3-dimensional (3D) approach to the description of synkinematic reactions and deformation microfabrics. In nature, garnet represents an extremely versatile recorder of metamorphism (Baxter & Scherer, 2013) and in particular garnet coronas capture metamorphic processes "in flagranti" (Carlson & Johnson, 1991; Carlson, 2011; Ague & Carlson, 2013). Consequently, garnet coronas and their metamorphic significance have been intensely studied over the past decades (Mørk, 1985; Johnson & Carlson, 1990; Johnson, 1993; Spiess *et al.*, 2001; Prior *et al.*, 2002; Konrad-Schmolke *et al.*, 2005; Massey *et al.*, 2011; Goergen & Whitney, 2012). Garnet porphyroblasts often hold the key to unravel the synkinematic PTtd conditions. The origin of these garnet porphyroblasts has been controversially discussed as either being evidence of rotational strains ("*Snowball garnets*", Johnson, 1993; Jiang & Williams, 2004), as documenting strain partitioning (Bell & Johnson, 1989; Aerden, 2005) or, where polycrystalline, as forming from the coalescence of nuclei (Spear & Daniel 2000, Spiess *et al.*, 2001, Dobbs *et al.* 2003, Hirsch *et al.* 2003, Whitney *et al.* 2008, Whitney *et al.* 2010). Garnet also readily partakes in mylonitic deformation: crystal plastic deformation of garnets at lower crustal conditions was documented by, e.g., Ji & Martignole (1994), Ji & Martignole (1996), Prior *et al.*, (2002), Storey & Prior (2005), Bestmann *et al.* (2008) Massey *et al.*(2011), Martelat *et al.*, (2012). Garnets in mylonitic eclogites from SW Norway were shown to have deformed by grain-boundary diffusion creep and by pressure-solution (Smit *et al.*, 2011). However, garnet in eclogitic mylonitized micaschists was also

shown to have deformed by cataclasis and frictional sliding (Trepmann & Stöckhert, 2002). Conclusions derived in these studies often invoke an extrapolation from the second to the third spatial dimension, which is naturally speculative. With the advent of X-ray microtomography, garnet became the focus of a number of microstructural studies that explored the third spatial dimension (Denison & Carlson, 1997; Ketcham, 2005a; Whitney *et al.*, 2008; Goergen & Whitney, 2012).

These pioneering 3-dimensional studies outlined the possibilities that the combination of X-ray microtomographic data with other microanalytical techniques holds in regards to the interrogation of tectono-metamorphic processes. In this present contribution, we apply this approach to analyse the distribution of garnet in rock samples from Kråkeneset, a tectonic domain within the well-studied Western Gneiss Region (Norway) (Mørk, 1985; Mørk, 1986; Austrheim, 1987; Boundy *et al.*, 1992; Austrheim *et al.*, 1997; Krabbendam & Dewey, 1998; Cuthbert *et al.*, 2000; Engvik *et al.*, 2000; Krabbendam *et al.*, 2000; Engvik *et al.*, 2001; Wain *et al.*, 2001; Labrousse *et al.*, 2004; Terry & Heidelbach, 2006; John *et al.*, 2009; Hacker & Andersen, 2010; Labrousse *et al.*, 2010). There, fluid infiltration along precursor fractures led to the eclogitization and coeval mylonitic overprint of gabbroic rocks (Mørk, 1985; Austrheim *et al.*, 1997; Krabbendam *et al.*, 2000; Engvik *et al.*, 2001; Lund & Austrheim, 2003; John *et al.*, 2009; Müller, 2013). Our field location is a gabbroic body in which hydrous eclogite-facies shear zones cross cut the almost pristine magmatic rock. There, reaction textures indicate that the eclogite-facies overprint is caused by the ingress of reactive fluids that helped to overcome sluggish reaction kinetics (Austrheim, 1987; Krabbendam *et al.*, 2000; Lund & Austrheim, 2003; John *et al.*, 2009; Müller, 2013). The rock samples cover a strain gradient (which we consider the 4th dimension) into a dm-scale mylonitic shear zone and document the metamorphic overprint. The strain gradient across the shear zones is ideally suited for such a study, in that it shows progressive deformation localization under well constrained P-T-fluids conditions. Based on the assumption that the strain gradient can be regarded as a proxy for time, which is a common assumption where strain softening leads to progressive strain localisation (Means, 1995; Fusses, *et al.*, 2006; Fusses & Handy, 2008), the samples allow us to characterize the spatiotemporal evolution of a gabbro into a deformed eclogite. In our samples, this transition is reflected by the evolving 3-dimensional distribution of garnets in the microfabric. We determine how the garnet evolved from its arrangement in a primary coronitic texture to forming a key component of the tectonic microfabric. To do this, we developed a methodological workflow that combined classical electron-beam techniques with synchrotron X-ray microtomography. In combination, these data allow us to speculate on the mechanisms that accomplished the transformation of garnet microfabrics.

GEOLOGICAL SETTING

The studied rock samples come from Kråkeneset in the Western Gneiss Region (WGR) of the Norwegian Caledonides. As in many other parts of this lowest tectonic unit in the Scandinavian terrains, the outcrops in Kråkeneset preserve evidence for Caledonian high-pressure metamorphism (P=2.0-2.4 GPa, T=710 °C- 800 °C) in association with the subduction of Baltica underneath Laurentia after the Silurian closure of the Iapetus ocean (Engvik, *et al.*, 2000; Krabbendam *et al.*, 2000; Wain *et al.*, 2001; Lund & Austrheim, 2003; Labrousse *et al.*, 2004; John *et al.*, 2009; Müller, 2013). It is commonly accepted that even though some of the rocks in the WGR were subducted to depths beyond 100 km, large parts

of the complex remained metastable until fluid infiltration along brittle fractures and cleavage planes overcame sluggish reaction kinetics and initiated large-scale eclogitisation (Austrheim, 1987; Krabbendam *et al.*, 2000; Wain *et al.*, 2001; Labrousse *et al.*, 2010). In Kråkeneset, the high-pressure metamorphic overprint takes the form of hydrous eclogites ($P=2.8-3.0$ GPa, $T=790^{\circ}\text{C}-850^{\circ}\text{C}$) that occur within shear zones cutting dry gabbroic host rocks (Krabbendam, *et al.*, 2000; Lund & Austrheim, 2003; John *et al.*, 2009). The pristine gabbroic mineral assemblage is preserved in the less deformed areas, and is characterized by an ophitic texture. However, olivine cores are surrounded by garnet and orthopyroxene coronas. The eclogite-facies mineral assemblages occur within narrow shear zones where, across their margin, a gradient from a “dry” gabbroic mineral assemblage (Ol + Cpx + Grt + Pl + Ilm + Bt + Am \pm Rt), to a synkinematic mostly “wet” eclogitic mineral assemblage is preserved. The latter consists of Grt + Opx + Am + Ab-Czo symplectites + Bt + Opaque phases (e. g Ilm) \pm phengite, as well as omphacite + garnet (Fig. 4), where the reaction advanced further or local chemical domains supported this assemblage (Austrheim, 1987; Lund & Austrheim, 2003; John *et al.*, 2009; Putnis & Austrheim, 2010; Müller, 2013). The replacement of magmatic plagioclase by Ab-Czo symplectites (e.g., Wayte *et al.*, 1989), along with the widespread formation of amphiboles and of Grt-Omp assemblages, occurs where transport during reactions has been enhanced (e.g., Mørk, 1985; John & Schenk, 2003; Putnis & Austrheim, 2010). All these developments positively correlate with the observed strain gradient, and show that eclogitization of the gabbro was driven by the close interplay of infiltration of externally derived fluids and deformation (Mørk, 1985; Austrheim, 1987; Krabbendam *et al.*, 2000; Lund & Austrheim, 2003; Labrousse *et al.*, 2010; Putnis & John, 2010).

METHODS

From a hand specimen that covers the margin of an eclogite shear zone, three 2-mm thick rock wafers covering the strain gradient were extracted in x-z kinematic orientations (Fig. 1). From these wafers, parallelepipeds with dimensions of 2x2x6 mm were cut for synchrotron X-ray microtomography ($S_{\mu}\text{CT}$). After $S_{\mu}\text{CT}$, the wafers including the $S_{\mu}\text{CT}$ samples were polished into thin sections that could be used for further analyses using light microscopy, scanning electron microscopy (SEM), electron microprobe analyses (EMPA) and electron backscatter diffraction (EBSD). This approach allowed for a comprehensive characterisation of the metamorphic microfabrics in four dimensions (Fig. 1). This study focussed on three specimens, #066B2, #061751 and #0618, which sample the low-, intermediate- and high-strain domains of the shear zone.

Analytical Techniques

Mineral assemblage and chemical zoning were analysed on the carbon-coated thin sections using a Zeiss SIGMA HD VP Field Emission SEM equipped with an Oxford Instruments SD Energy-dispersive X-ray Spectroscopy (EDS) detector and AZtec software for acquisition and processing of EDS spectra, at the School of Geoscience in Edinburgh. Working conditions during acquisition of SEM backscatter images and during EDS analysis were 20 kV acceleration voltage and a working distance of 6.9 mm. Chemical compositions, to be correlated with the X-ray absorption coefficients, were measured on a Cameca SX100

electron microprobe at 20 kV acceleration voltage and a beam diameter of 3 μm , at the University of Edinburgh. Further microprobe analyses were acquired at the EMPA at the University of Munster, using a JEOL 8530F electron microprobe. The standard microprobe conditions were 15 nA and 20 kV for quantitative analysis and 50 nA and 15 kV for the element mapping. Compositional maps were obtained using XMapTools v. 2.3.1 (Lanari *et al.*, 2014).

Crystallographic orientations were measured on a Jeol 6610 SEM equipped with a NordlysNano EBSD detector (Oxford Instruments) at the Plymouth University Electron Microscopy Centre. Working conditions during acquisition of the EBSD patterns were 20 kV acceleration voltage, 70° sample tilt, high vacuum (in case of the carbon-coated samples 0617 and 066B2), and low vacuum (30 Pa, in case of the uncoated sample 0618). EBSD patterns were acquired on rectangular grids with step sizes varying from 0.8 to 4.8 μm . All the thin sections were chemically polished with colloidal silica prior to EBSD analysis. EBSD patterns were indexed with the AZtec software (Oxford Instruments) and processed with Channel 5 software (Oxford Instruments). Raw EBSD data were processed to reduce data noise following the procedure proposed by Prior *et al.*, (2002) and Bestmann & Prior (2003). Crystallographic data were plotted on pole figures as one point per grain. Pole figures are oriented with their horizontal diameter corresponding to the trace of the mylonitic foliation (E-W). Crystallographic maps were produced to highlight phase distribution (phase map), the internal misorientation of grains (local misorientation map) and the crystallographic orientation of grains with respect to specific directions in the kinematic reference frame (Inverse Pole Figure Map, IPF).

Synchrotron X-ray microtomography

X-ray absorption microtomographic data were collected at the beamline 2-BM at the Advanced Photon Source (USA) using a monochromatic beam of 27 KeV and a low sample-detector distance to minimise phase contrast. 1500 projections per dataset were reconstructed into 3-dimensional image stacks using the gridrec algorithm (Rivers & Wang, 2006). The voxel (i.e. a 3-dimensional pixel) side length of the reconstructed data is 1.3 μm , which is sufficient to resolve the necessary petrographic details on the μm -scale.

Image Processing and Analysis

The reconstructed X-ray absorption microtomographic datasets were filtered using an Anisotropic Diffusion Filter 2D to reduce image noise (Tschumperlé & Deriche, 2005; Schlüter *et al.*, 2014). Using the image processing software Fiji (Schindelin *et al.*, 2012), garnet was then segmented (i.e. numerically isolated) from the 3-dimensional data using Statistical Region Merging followed by Global Thresholding (Nock & Nielsen, 2004) (see supp. information, Appendix S2). Analysis of the resulting segmented images included the quantification of garnet volumes and grain sizes, as well as a garnet interconnectivity analysis, all of which were performed in Avizo Fire (v.8) (<http://www.fei.com/software/avizo3d/>) using its Labelling and Label Analysis operators. Label analysis is a process that identifies and evaluates face-connected clusters of voxels belonging to a specific class (i.e. garnet) in segmented data. Face-connected voxel clusters do not represent individual garnet grains but rather volumes occupied by garnet. Since X-ray absorption microtomography does not detect grain boundaries in the garnet coronas,

numerical separation of the voxel clusters into individual grains is impossible in our data and we are restricted to interpreting voxel clusters. To avoid introducing numerical artefacts derived from segmentation errors during the analyses of garnet, isolated voxel clusters with a volume smaller than 125 cubic voxels ($5 \times 5 \times 5$ voxels, $\sim 275 \mu\text{m}^3$) were removed using the Analysis Filter operator (see Füsseis *et al.*, 2012 for details).

In microtomographic data, volume calculations are affected by errors introduced by the segmentation method (Arns *et al.*, 2002). To estimate the errors, we applied the method described in Füsseis *et al.* (2012). Each segmented volume was both numerically eroded and dilated by 1 voxel, and the resulting changes to the volume and label analysis were quantified. The resulting quantifications are considered as maximum possible errors. Besides providing error bars, binary data that have been eroded or dilated have the potential to reveal details on the shape and spatial arrangement of voxel clusters, as each morphological operation (numerical erosion) will cause voxel clusters to join, break up or disappear altogether (see inset in Fig. 8). We analysed a version of the segmented garnet data that underwent a single morphological erosion step. Morphological erosion removes each voxel classified as garnet that is not completely surrounded by other voxels classified the same. The erosion operator responds to the size and shape of the voxel clusters, and the shortest diameter defines this response. The smallest unit that would survive a morphological erosion step is a cubic array consisting of 3^3 voxels. A much larger, spherical voxel cluster would retain its spherical shape through multiple erosion steps. Oblate voxel clusters will respond differently to erosion. Where cluster shapes are irregular, morphological erosion will stragulate clusters at the weakest links and break them apart into several smaller ones, which is reflected by a corresponding change in the cluster size distribution.

Using Avizo Fire, the 2-dimensional BSE images together with the EDS and EBSD image data were reintroduced into 3-dimensional space to combine observations from various sources with the microtomographic data into multidimensional datasets (Fig. 2 & 3). This allowed correlating X-ray absorption signals with chemical compositions and crystallographic information and, as a result, extrapolating observations made by electron microscopy to the third dimension (see supp. information, Appendix S1).

RESULTS

Petrological characterization

In the *low strain domain*, at larger distance to the shear zone centre (sample #066B2), although the magmatic gabbroic assemblage is still preserved, all mineral phases show reaction textures (Fig. 3a). These reactions, related to sluggish kinetics, were triggered by fluid-rock interactions: the amount of the reacted rock volume decreases with the distance to the hydrous shear zone (Lund & Austrheim, 2003; John *et al.*, 2009).

Olivine cores ($\text{Fo}_{54}\text{Fa}_{45.6}\text{Tep}_{0.3}$) are surrounded by innermost coronas of fibrous orthopyroxene followed by a $\sim 50 \mu\text{m}$ wide poikiloblastic corona of garnet ($\text{Alm}_{63.3}\text{Grs}_{19.8}\text{Py}_{14.9}$, Fig. 3a) and fibrous amphibole (hornblende) at the contact with plagioclase. The grain size of olivine cores is variable, generally of the order of a few hundred micrometers. Olivine grains exhibit cleavage planes in different orientations. While orthopyroxene coronas seem to have a constant width around olivine grains, garnet coronas

vary in thickness. Biotite is present in the mineralogical assemblage as stand-alone grains. These microfabrics are similar to the ones previously described by Mørk, (1985), Krabbendam *et al.*, (2000), Lund & Austrheim (2003), Müller (2013).

In the *intermediate strain domain* (sample #061751), the assemblage changes (Fig. 3c-3d). Olivine grains are pseudomorphically replaced by orthopyroxene and orthoamphibole intergrowth, which is surrounded by a thin (a few μm wide) rim of omphacite (Fig. 4b, see also Lund & Austrheim, 2003). Clinopyroxene grains in this domain appear less regular and altered by cloudy patches of Fe-Ti oxides as a result of destabilization through the reaction: $\text{Cpx (Aug)} + \text{Na} \Rightarrow \text{Na-Aug} + \text{Fe-Ti oxides}$, in which Na-Aug constitutes a second generation of more altered clinopyroxene with increase Jd-component but reduced Ti and Fe contents (Cpx_2) (Mørk, 1985). Garnet and amphibole are still present, but they do not form clear corona structures anymore (see also Fig. 3c). The 3-dimensional distribution of garnets still resemble coronas where decaying olivine grains are more completely replaced by orthopyroxene, but generally garnet grains develop euhedral crystals and form disconnected and more elongated aggregates (Fig. 7b). Towards the shear zone, all plagioclase is replaced by clinozoisite and albite symplectites through the reaction (Fig. 4b, c): $\text{Pl (An)} + \text{H}_2\text{O} \Rightarrow \text{Czo} + \text{Ab symplectites}$ (Wayte *et al.*, 1989; Lund & Austrheim, 2003; John *et al.*, 2009; Müller, 2013) (Fig. 4).

In the *most deformed sample* (#0618), all mineral phases are aligned parallel to a mylonitic foliation. The foliation is defined by a compositional layering of elongated orthopyroxene-amphibole symplectites, and garnet, forming isolated elongated clusters $>100 \mu\text{m}$ wide and several hundred μm long (Fig. 3e-3f). Some of the garnet grains still exhibit faceted crystals (Fig. 7c).

Omphacite is present at the margins of relict magmatic clinopyroxene grains and of orthopyroxene-amphibole symplectites (Fig. 4c).

Garnet chemical composition

Garnet compositions in the three samples were measured using electron microprobe analyses in order to confirm the chemical evolution of garnet with respect to the deformation history (Fig. 5, 6). With increasing deformation, garnet compositions become more Alm-rich (Fig. 5), an expected trend for a gabbro that is gradually equilibrating under eclogite-facies P-T conditions. Within the low-strain domain, high CaO concentrations (X_{Grs}) are represented by garnet in the proximity of Ca-rich phases (e.g. plagioclase). In the high strain domain the compositional maps show that some garnet displays CaO zoning (5-12 wt. %) and MgO zoning pattern similar to those observed in low strain domain (Fig. 6). Many garnets, however, have low CaO, reflecting an equilibration towards Alm-rich compositions. Nevertheless, some grain do have a higher content in CaO ($\sim 10\%$) (a') and MgO ($\sim 11\%$) (b'). We interpret this to result from coalescence (a, b) and subsequent disintegration of individual zoned coronas. Furthermore, fine-grained garnets (Fig. 6c to the left) represent highly fragmented and collapsed former coronas.

4D spatial evolution of garnet grains

A subvolume with dimensions of 600^3 voxels ($\sim 0.5 \text{ mm}^3$) was extracted from each of the

three microtomographic datasets to visualize the 3-dimensional distribution of garnet (Fig. 7). In the subsequent label analysis, garnet distribution was evaluated and quantified in the original, statistically representative 7 mm³ subvolumes (Fig. 3, 10). In the label analysis, we considered all garnet clusters that consist of face-connected voxels and are larger than 125 cubic voxels ($\sim 275 \mu\text{m}^3$). This allowed us to relate the following observations to the 3-dimensional petrography presented above.

The volumetric quantification of the segmented garnet data shows that the garnet volume increases into the shear zone, from 6 % (± 2.5 %) in the low-strain sample, to 11 % (± 3 %) in the intermediate strain sample, and 20 % (± 4 %) in the high-strain sample.

The visualisation confirms that in the *low strain domain*, garnet forms voluminous interconnected coronas around orthopyroxene and decaying olivine grains (Fig. 7). It also becomes apparent that different olivine cores have garnet rims with different thicknesses. Measurements of garnet corona thicknesses around five different olivine grains show an average thickness of 60 μm with standard deviations that vary from 10 to 35 μm in the most complex coronas. Where two olivine grains neighbour each other, garnet coronas become almost twice as thick. There seems to be no correlation between the thickness of the garnet- and the amphibole rims, which should have evolved in unison (Mørk, 1985; Mørk, 1986; Johnson & Carlson, 1990). Despite their considerable spatial extent, garnet coronas do not enclose olivine grains entirely, which leaves dormant reactants in direct contact with each other (Figure 9). The resulting baseball-glove shaped domains also do not show any preferential spatial orientation with respect to the kinematic framework of the shear zone (Figure 10). The total garnet volume in the analysed subvolume is accommodated by 1116 garnet voxel clusters (Table S3).

The label analysis shows that the garnet population is dominated by one large interconnected garnet voxel cluster that percolates across the entire subvolume (Fig. 10a). This cluster accounts for 83 % of the entire garnet volume in the sample (Fig. 8a, B). Garnet voxel clusters between $2.2 \cdot 10^6$ and $3.08 \cdot 10^7 \mu\text{m}^3$ account for 11%, whereas voxel clusters $< 2.2 \cdot 10^6 \mu\text{m}^3$ do not contribute substantially to the total garnet volume (Fig. 8b).

We submitted the segmented data to a numerical volume erosion process to learn more about the spatial arrangement of garnet (see supporting information for details on the procedure and Table S4 for the results). Garnet interconnectivity persists through the volume erosion, which evidences how tightly individual garnets grains are linked in the coronas (see supp. information for details). In the eroded data, the garnet volume forms 2796 voxel clusters (Table S4). The largest interconnected voxel cluster dramatically decreases in volume from $4 \cdot 10^8 \mu\text{m}^3$ to $10^8 \mu\text{m}^3$, now accounting for only 35 % of the total volume. The eight largest interconnected voxel clusters ($> 2.2 \cdot 10^6 \mu\text{m}^3$) account for 89 % of the total garnet volume as seen in the cumulative frequency diagram (Fig. 8b). The erosion process also leads to a substantial increase in frequency for sizes smaller than 10^4 cubic μm^3 (Fig. 8a), which is in contrast to the intermediate and high-strain datasets.

The visualisation of garnet in the *intermediate strain domain* shows that the larger garnet voxel clusters form complexly-shaped rims around orthopyroxene aggregates that likely have their origin in former coronas (Fig. 10b). In this sample, the garnet volume is made up of 12068 garnet voxel clusters. This almost ten-fold increase over the low strain sample is essentially being accommodated by the smallest ($< 10^5 \mu\text{m}^3$) and largest ($> 6 \cdot 10^8 \mu\text{m}^3$) voxel cluster size fractions (Table S3). A similar number of voxel clusters in the size region of 10^5

μm^3 was detected, whilst a particularly large number of voxel clusters with volumes between 10^3 and $10^4 \mu\text{m}^3$ were found. Again, the largest 10 voxel clusters ($> 2.2 \cdot 10^6 \mu\text{m}^3$) account for over 90 % of the total garnet volume. The largest interconnected voxel cluster, which is larger than in the low-strain sample (from $4 \cdot 10^8 \mu\text{m}^3$ to $6.5 \cdot 10^8 \mu\text{m}^3$), develops through the subvolume and accounts for 80 % of the total garnet volume. The garnet voxel clusters in the range of $2.6 \cdot 10^5$ to $4 \cdot 10^6 \mu\text{m}^3$ are often formed by isolated, euhedral and potentially newly formed garnet grains (Fig. 7, 10b; see Discussion). Voxel clusters smaller than $10^5 \mu\text{m}^3$ are arranged in patchy clouds surrounding bigger interconnected voxel clusters.

In the numerically eroded data, the number of garnet voxel cluster reduces to 4995. Since a numerical erosion cannot lead to voxel cluster coalescence, this decrease reflects a sensitivity to the disappearance of volumetrically small voxel clusters in the procedure (Fig. 8c, Table S4). In the erosion process, the largest voxel cluster breaks apart to form two smaller voxel clusters, which together account for 70 % of total garnet volume (Fig. 8d, Fig. S9).

In the *most deformed sample*, the garnet voxel clusters define a mylonitic foliation. In this subvolume, garnets contribute to a deformation microfabric; the garnet voxel clusters define the compositional layering observed in the SEM analysis (Fig. 10c). Additional analyses that we conducted (using the software package Quant3D, Ketcham & Ryan (2004)) revealed that most of the garnet voxel clusters in this sample have an oblate shape (Fig. S11). Garnet in the subvolume is organized in 9297 voxel clusters (Table S3). A total of 46 voxel clusters have a volume larger than $2.2 \cdot 10^6 \mu\text{m}^3$, and they account for 86 % of the total garnet volume (Fig. 8f). The absolute frequency-size distribution is self-similar, with no major local variations between the size classes. This trend is confirmed by the cumulative plot (Fig. 8f), which shows that all size classes contribute progressively towards the total garnet volume, and is in contrast to the other two samples.

Numerical erosion reduces the number of garnet voxel clusters to 8014, of which 62 are larger than $2.2 \cdot 10^6 \mu\text{m}^3$ and accommodate 81 % of garnet total volume (Table S4). The reduction in total voxel cluster number is accommodated by all size fractions, which indicates that the voxel clusters have shapes that withstand a numerical erosion process (Fig. 8e, f).

EBSD analysis: Misorientation of garnet grains in the shear zone

We analysed predominantly garnet in the three samples using EBSD to investigate the dominant deformation mechanisms that contributed towards the evolution of the microfabric in garnets.

Garnet and orthopyroxene in the *low strain sample* exhibit frequent low angle boundaries (misorientation between 3° and 10°). The phase map of a coronitic domain around magmatic olivine shows that orthopyroxene and hornblende grows as fibrous crystals: the long axis of orthopyroxene and hornblende are perpendicular to the reaction interface (Fig. S3a). In the case of hornblende, the elongation is parallel to the $\langle 001 \rangle$ axis (Fig. S4f). The inverse pole figure map (IPF) of garnet, shown with respect to the E-W direction (i.e. approximately equivalent to the normal to the reaction interface and parallel to the elongation direction of hornblende) (Fig. 11a), highlights the presence of low-angle boundaries, which correspond, in the local misorientation map (Fig. S3c), to internal misorientation zones with up to 9° of misorientation in garnet. A misorientation profile across them does not show any progressive distortion of the crystal lattice, but rather a sudden jump in misorientation (Fig. 11b). The average local internal misorientation of

grains is very low, on the order of 1° , i.e. within the error of measurement. The misorientation axes for misorientation angles of $3\text{--}10^\circ$ do not show clear maxima in crystal coordinates (Fig. 11c). Differently from orthopyroxene and amphibole, garnet does not show a clear preferred orientation with respect to the reaction interface (Fig. 11a, S4e). In the *intermediate strain sample* the spatial density of low angle boundaries is highly variable. A local misorientation map shows that the interiors of garnet grains are virtually undeformed (average local misorientation on the order of 1°), and that there are bands with high misorientation up to 9° (Fig. S5b). A misorientation profile across one of the bands shows a rather abrupt misorientation jump (of up to 8°) (Figure 11e). Similar to the low strain domain, the misorientation axes for misorientation angles of $3\text{--}10^\circ$ do not show clear maxima in crystal coordinates (Figure 11f). The IPF map and the associated pole figures show a weak preferred orientation of garnet, with clusters of grains preferentially oriented with their $\langle 111 \rangle$ parallel to the stretching lineation of the shear zone (Fig. S5a, S5e). The IPF map shows that garnet grains range in size between $10\text{--}20\ \mu\text{m}$ and $200\ \mu\text{m}$. In the *high strain sample*, the density of low angle boundaries in garnet is very low, and they are typically present only in grains larger than $50\ \mu\text{m}$ (Figure 11G). The phase map indicates that individual garnet grains range in size from ca. $10\ \mu\text{m}$ to ca. $150\text{--}200\ \mu\text{m}$ and are dispersed in a matrix of hornblende, orthopyroxene and minor biotite (Fig. S6a). Garnet grains are internally strain-free (average local misorientation is $< 1^\circ$), and again, there is no progressive accumulation of misorientation towards the few internal high misorientation bands (as indicated by the local misorientation map in Fig. S6b). Less frequently, a progressive accumulation of lattice distortion (of up to 4°) towards the low angle boundaries was observed (Fig. 11h). The misorientation axes for misorientation angles of $3\text{--}10^\circ$ do not show clear maxima in crystal coordinates (Fig. 11i). Pole figures of garnet show only weak maxima of $\langle 100 \rangle$, one of which is oriented subparallel to the stretching lineation (Fig. S6c, S7a, S7b). Neighbouring grains are typically characterized by large misorientations ($> 30^\circ$, Fig. S6f). In contrast, hornblende shows a crystal preferred orientation (CPO) with the c-axis oriented subparallel to the stretching lineation. This CPO of hornblende has been commonly observed in lower crustal shear zones where hornblende grew synkinematically to deformation (Berger & Stünitz, 1996; Getsinger & Hirth, 2014; Menegon *et al.*, 2015).

DISCUSSION

Synkinematic nature of fluid-rock interaction

According to Mørk (1985), the coronas between olivine and plagioclase form through reaction: $\text{Ol} + \text{Pl} (\text{An}) + \text{Cpx} + \text{H}_2\text{O} \Rightarrow \text{Opx} + \text{Grt} + \text{Am} + \text{Pl} (\text{Ab})$. It is unclear whether these coronas formed as products of synkinematic fluid infiltration (Krabbendam *et al.*, 2000; Lund & Austrheim, 2003), or as results of late-magmatic processes (Mørk, 1986). However, we speculate that amphibole is indicative of the external influx of hydrous fluids upon shear zone formation, as shown later by CPO of hornblende in the high strain zone (Austrheim, 1987; Austrheim, *et al.*, 1997; Engvik *et al.*, 2000; Labrousse *et al.*, 2004; Putnis & Austrheim, 2010).

Moreover, truly eclogite-facies assemblages are only observed at fluid pathways terminations or where fluid availability and/or deformation enhanced the size of the reacted

domains allowing for sufficient material transport and thus bulk equilibration resulting in the formation of an omphacite-garnet assemblage (Fig. 4) (Lund & Austrheim, 2003; John *et al.*, 2009; Putnis & Austrheim, 2010). However, the overall dominance of amphibole over omphacite in the samples indicates that the chemical equilibrium of the system was local, and in favour of garnet-amphibole assemblage, instead of garnet and omphacite. In those cases where plagioclase reacted in rather isochemical systems, the high-pressure assemblage is dominated by the Ab-Czo symplectites \pm amphibole \pm garnet as reported by Lund & Austrheim (2003) and John *et al.* (2009).

Mørk (1985) interprets the discontinuous growth of thin omphacite layers between orthopyroxene and garnet coronas to have formed through: $(Ol) + Grt + Opx + Am + Pl \Rightarrow Omp + Spl$. However, the lack of spinel inclusions observed by Mørk (1985) points to this reaction being incomplete in our samples, and mineral growth limited by material supply (see also Mørk, 1985; John *et al.*, 2009). The Ab-Czo symplectites are preserved without evidence of any later overprint, and we consider them to have formed as prograde replacement of plagioclase in a fluid-mediated system, indicating a metastable prograde reaction (Wayte *et al.*, 1989). Therefore, in the presence of amphibole, omphacite associated with these delicate symplectite textures indicates a prograde conversion of the gabbro to an eclogite in which fluid infiltration was synkinematic and linked to the progress of reaction and deformation (Fig. 4b).

Strain-dependent evolution of garnet microfabrics in the Kråkeneset shear zone

The observations reported above allow to draw a detailed picture of the synkinematic evolution of garnet in this deep-crustal shear zone. Our microtomographic data indicate that, across the studied shear zone margin, from low to high strain, garnets evolve from a highly interconnected coronitic texture to a tectonic microfabric, where they are organized in oblate aggregates and define the foliation of the shear zone (Fig. 10c). Simultaneously, the garnet volume in the rocks more than triples. Based on chemical analyses, which revealed a partial local equilibration of garnets grains at eclogite facies (Fe-rich), we interpret the oblate sheared aggregates as having formed by the progressive, synkinematic disintegration and rearrangement of coronas in combination with the simultaneous nucleation and coalescence of garnets grains at similar P, T, X metamorphic conditions (Fig. 12).

We argue that the garnet coronas originally formed as the high-pressure reaction products of a prograde metastable reaction between olivine and plagioclase by the coalescence of nuclei. As strain localises in the shear zone, these garnet coronas are broken apart and start to disintegrate (Fig. 12a, 12b). At this stage, the garnet voxel clusters do not reflect a deformation microfabric yet, and the largest garnet cluster is still interconnected through the entire sample forming complexly-shaped rims around orthopyroxene porphyroclasts that have replaced olivine. New garnet grains nucleate in between these large voxel clusters but are still small at this stage, while existing garnet grains are overgrown and increase in volume. At the highest level of strain, the former garnet coronas have been deformed and re-arranged by granular flow in a ductively deforming matrix, leading to a mylonitic deformation microfabrics defined by oblate garnet voxel clusters (Fig. 3, 10c).

What happens to the garnet?

The results of the label analysis, and in particular the evolution of different size classes of garnet voxel clusters, reveal how the volumetric increase in garnet is accommodated and

what processes affect the garnet population across the shear zone margin. The overall increase in the number of garnet voxel clusters into the shear zone reflects the synkinematic formation of a well-dispersed garnet population (Fig. 8). This is achieved by the coeval activity of three processes, the fragmentation and breakup of garnet coronas, the formation of overgrowth rims, and the nucleation of new garnet crystals (Fig. 12):

1. The increase in the number of garnet voxel clusters, particularly the large ones, with increasing strain clearly reflects a reduction of garnet interconnectivity. The largest voxel cluster in the low and intermediate strain domain accounts for ~80 % of the overall garnet volume, whereas a similar volume proportion is accommodated by 46 voxel clusters ($> 2.2 \cdot 10^6 \mu\text{m}^3$) in the most deformed sample.
2. The transition from the low strain- to the intermediate strain domain sees a complete reorganisation in the population of the smallest garnet voxel clusters (Fig. 8c). Voxel clusters $\leq 4.1 \cdot 10^3 \mu\text{m}^3$ increase in number from 698 to 11239 (Table S3). These clusters occur dispersed in between the larger clusters, without any obvious textural link. As the total amount of garnet volume increases, they cannot be fragments of initial coronitic garnet, therefore we argue that this population of smallest voxel clusters is the product of nucleation and speculate that these garnets may evidence pervasive fluid infiltration (see following section).
3. In contrast, we infer the increase in the number of intermediate-sized voxel clusters with volumes between $2.6 \cdot 10^5$ and $4 \cdot 10^6 \mu\text{m}^3$, which is particularly apparent in the intermediate strain domain, to be related to overgrowth. The 3-dimensional visualisation shows that garnet voxel clusters have euhedral or semi-euhedral shapes, which is congruent with this mechanism (Padrón-Navarta *et al.*, 2008).

What the morphological operator “Erosion” reveals about the garnet distribution

The frequency diagrams reveal that the number of voxel clusters does increase as a response to erosion in the *low strain domain* for smaller voxel cluster sizes ($< 10^4 \mu\text{m}^3$, Fig. 8a, b) and in the *intermediate strain domain* for the largest interconnected cluster (Fig. 9). This indicates that a substantial number of voxel clusters exhibit cross-sectional diameters short enough to respond to a single erosion step. By acting as predetermined breaking points, these weak bridges become crucial in the disintegration of the garnet coronas as the rock transitions to the intermediate strain microfabrics (see also Fig. 12a). We infer that the larger proportion of the garnet volume that is accommodated by smaller clusters in the eroded dataset (Fig. 8b) is a consequence of this break-up.

In the *intermediate strain domain*, the absolute frequency of voxel clusters $< 5 \cdot 10^4 \mu\text{m}^3$ decreases significantly as a consequence of morphological erosion (Figure 8c, Tables S3, S4). These are the voxel clusters that make up the patchy clouds in between the larger garnet aggregates. Many of these small clusters are apparently susceptible to annihilation in a single erosion step, which points towards a significant deviation from sphericity in this voxel cluster population.

In the *high strain domain*, the garnet voxel clusters retain their self-similar frequency-size distribution through the morphological erosion process in the high strain domain (Fig. 8e, f). However, the changes to the frequency of voxel clusters in the different bins seem to reflect a slight decrease in the fractal dimension (Fig. 8e, f). A new population of voxel clusters with volumes $< 10^3 \mu\text{m}^3$ is generated from larger clusters, and the largest voxel cluster halves

in size (from 1.1 to $2.2 \cdot 10^8 \mu\text{m}^3$).

Micromechanisms involved

Our EBSD data indicate that the mechanism by which the garnet coronas are disintegrated does not involve crystal plasticity by means of dislocation activity. Whilst garnet was shown to deform by dislocation creep at upper amphibolite to granulite facies metamorphic conditions (Ji & Martignole, 1994; Ji & Martignole, 1996), this was not the case in the sampled shear zone. Misorientation maps and profiles indicate that neighbouring garnet domains show only limited rotations (Fig. 11). These motions are accommodated by narrow, distinct bands that correspond to low-angle boundaries; the grains themselves show very little internal deformation. The bands coincide with sudden jumps in misorientations, testifying the lack of crystal plasticity (Fig. 11b, e, h, e.g. Viegas *et al.*, (2016)). Furthermore, the plots of misorientation axis in crystal coordinates show that the low-angle boundaries are not tied to the host crystallography but rather show a highly dispersed distribution (Fig. 11c, f, i). Based on these arguments, we suggest that the low angle boundaries in the low strain domain are growth features, and probably related to an early stage of coalescence of nuclei. The overall lack of chemical differences amongst the newly formed garnets and their seeds would be congruent with a close initial nucleation spacing of garnets seeds, similar to the observations reported in Whitney & Seaton (2010).

On the basis of an almost complete lack of evidence for crystal plasticity, we argue that the progressive disintegration and rearrangement of garnet coronas was accommodated by microfracturing and passive granular flow of garnets in a viscously deforming matrix (cfr. Trepmann & Stöckhert, 2002). This view is supported by experimental data on garnet rheology, which establish the possibility of brittle garnet behaviour at the inferred metamorphic conditions (Voegelé *et al.*, 1998; Wang & Ji, 1999; Zhang & Green, 2007).

Microfracturing and passive granular flow of garnet grains could have been assisted by a fluid phase (Den Brok & Kruhl, 1996; Storey & Prior, 2005; Smit *et al.*, 2011). As it is well established, fluid infiltration played a critical role in triggering eclogitization and strain localisation in dry and ridged precursor rocks (Austrheim, 1987; Austrheim *et al.*, 1997; Engvik *et al.*, 2000; John & Schenk, 2003; Miller *et al.*, 2007; Labrousse *et al.*, 2010; Putnis & John, 2010). The presence of fluids in the system is evident from the hydrous high-pressure mineral assemblage in the shear zone. However, we found no clear evidence for fluid-assisted deformation mechanisms, such as intergranular pressure solution (e. g. Azor *et al.*, (1997), Smit *et al.*, (2011)), diffusion creep (Den Brok & Kruhl, 1996; Storey & Prior, 2005) or grain-boundary sliding and diffusion creep (Terry & Heidelbach, 2004) to have dominated garnet deformation. However, we do interpret garnet to trace fluid migration pathways to some extent (see following subsection).

Implications for fluid flow, mass- and element transport

The 3-dimensional spatial arrangement of garnets is not only the result of deformation, but, in the low-strain domain, it also reflects mass transport between plagioclase and olivine grains during their reaction (Austrheim, 1987; Lund & Austrheim, 2003; Labrousse *et al.*, 2010; Putnis & John, 2010). Our observations show that garnet coronas are highly interconnected throughout the low strain samples (Fig. 10a) and thus, fluid transport must have happened on a trans-granular scale. However, the coronas do not encapsulate and isolate olivine grains from plagioclase, as commonly thought when observing coronas in

two dimensions (Mørk, 1986; Johnson & Carlson, 1990; Keller *et al.*, 2004). Where the coronas did not form, this happened despite the reactants being in direct contact with each other, and obviously the reaction was subdued. We argue that garnet formed where fluids facilitated the reaction and we therefore link the heterogeneously distributed reaction products to fossilized fluid pathways.

In the intermediate strain domain, syn-reactive fluid-infiltration is testified by the presence of cloudy patches of small garnets, along with the observation that water-bearing minerals are concentrated in the shear zone centre. The abundance of these minerals decreases along the lateral strain gradient away from the shear zone and are absent where the gabbro is undeformed (John *et al.*, 2009). These observations are congruent with those reported in earlier studies by Austrheim (1987), Wayte *et al.*, (1989), Engvik *et al.* (2001), John & Schenk (2003), and Putnis & John (2010). These studies established that eclogitization in the lower crust can be triggered by an external input of fluids and facilitated by the presence of preferential pathways, such as fractures, which controlled element mobility and defined reaction pathways. However, our data also reveal that there is no systematic arrangement of the garnet coronas with respect to a kinematic framework defined by the deformation microfabrics. It therefore remains unclear what controlled preferential fluid pathways on the grain scale.

In an extension to this argument, we claim that in the high-strain samples, the oblate garnet aggregates also should have channelized synkinematic fluid flow (see also Austrheim (1987)). We interpret the aligned, oblate garnet aggregates, defining the foliation, and thereby direct synkinematic fluid flow in the shear zone.

CONCLUSIONS

4-dimensional quantitative X-ray micro-tomography proved to be an excellent approach to investigate the evolution of metamorphic reaction microfabrics in three dimensions. In combination with established microanalytical methods, it allowed a comprehensive characterization of the processes affecting the evolution of garnet during eclogitization in a shear zone in the Western Gneiss Region, Norway. In particular, we were able to:

- Capture and monitor the spatial distribution of mineral phases in four dimensions: the X-ray absorption contrast between individual mineral phases in our micro-tomographic data is sufficient to allow the same petrographic observations than in light- and electron microscopy, but extended to the 3rd and, where strain is considered a proxy for time, 4th dimension.
- Quantify the change in garnet volume across the strain gradient: with increasing deformation, the garnet volume increases from about 6 % to 20 %.
- Determine the interconnectivity of garnet grains as a function of strain, with implication for mass transport, syn-reactive fluid flow and rock strength.
- Identify the 3-dimensional geometry of garnet coronas, find that they do not encapsulate olivine grains and have no apparent preferred alignment. We interpret the garnet coronas to

outline fossilized fluid pathways.

- Identify the mechanisms by which garnet is reorganised during shearing: microfracturing, nucleation and overgrowth. We interpret these observations as pointing to a mechanical disintegration of garnet coronas during strain localisation and their rearrangement into individual sheared isolated voxel clusters, with the ongoing nucleation of new garnets and overgrowth while the rock was deforming. There is no evidence for crystal plastic deformation, all garnets are internally strain free and in the more deformed samples they show a very weak crystal preferred orientation.

Our study clearly shows what 3- or 4-dimensional datasets from reaction micro-fabrics can add to the understanding of metamorphic processes. We reiterate that a 2-dimensional analysis of deformation microfabrics can lead to incorrect petrological and structural interpretations, and it does omit information that only become available when rocks are investigated in three dimensions.

ACKNOWLEDGEMENTS

The authors would like to thank Dr Simona Hapca (University of Dundee), for useful suggestions on garnet segmentation, and Dr Stephen Centrella (University of Münster) for acquiring the new EMPA analyses. LM acknowledges financial support from a FP7 Marie Curie Career Integration Grant (grant agreement PCIG13-GA-2013-618289). The staff at the Plymouth University Electron Microscopy Centre is thanked for support during EBSD analysis. We also would like to thank the reviewers for the extensive suggestions and helpful comments to improve the manuscript. Finally, we declare we do not have any conflict of interest.

REFERENCES

- Aerden, D., 2005. Comment on “Reference frame, angular momentum, and porphyroblast rotation” by Dazhi Jiang and Paul F. Williams. *Journal of Structural Geology*, **27**, 1128–1133.
- Ague, J.J. & Carlson, W.D., 2013. Metamorphism as garnet sees it: The kinetics of nucleation and growth, equilibration, and diffusional relaxation. *Elements*, **9**, 439–445.
- Arns, C.H., Knackstedt, M. a., Pinczewski, W.V. & Garboczi, E.J., 2002. Computation of linear elastic properties from microtomographic images: Methodology and agreement between theory and experiment. *Geophysics*, **67**, 1396.
- Austrheim, H., 1987. Eclogitization of lower crustal granulites by fluid migration through shear zones. *Earth and Planetary Science Letters*, **81**, 221–232.
- Austrheim, H., Erambert, M. & Engvik, A.K., 1997. Processing of crust in the root of the Caledonian continental collision zone: the role of eclogitization. *Tectonophysics*, **273**, 129–153.
- Azor, A., Simancas, J.F., Exposito, I., Lodeiro, F.G. & Martinez Poyatos, D.J., 1997. Deformation of garnets in a low-grade shear zone. *Journal of Structural Geology*, **19**, 1137–1148.
- Baxter, E.F. & Scherer, E.E., 2013. Garnet geochronology: Timekeeper of tectonometamorphic processes. *Elements*, **9**, 433–438.

- Bell, T.H. & Johnson, S.E., 1989. The role of deformation partitioning in the deformation and recrystallization of plagioclase and K-feldspar in the Woodroffe Thrust mylonite zone, central Australia. *Journal of Metamorphic Geology*, **7**, 151–168.
- Berger, A. & Stünitz, H., 1996. Deformation mechanisms and reaction of hornblende: examples from the Bergell tonalite (Central Alps). *Tectonophysics*, **257**, 149–174.
- Bestmann, M. & Prior, D.J., 2003. Intragranular dynamic recrystallization in naturally deformed calcite marble: Diffusion accommodated grain boundary sliding as a result of subgrain rotation recrystallization. *Journal of Structural Geology*, **25**, 1597–1613.
- Bestmann, M., Habler, G., Heidelbach, F., & Thoni, M., 2008. Dynamic recrystallization of garnet and related diffusion processes. *Journal of Structural Geology*, **30**, 777–790.
- Boundy, T.M. Fountain, D.M., & Austrheim, H., 1992. Structural development and petrofabrics of eclogite facies shear zones, Bergen Arcs, western Norway: implications for deep crustal deformational processes. *Journal of Metamorphic Geology*, **10**, 127–146.
- Den Brok, B. & Kruhl, J.H., 1996. Pergamon Ductility of garnet as an indicator of extremely high temperature deformation. *Journal of Structural Geology*, **16**, 985–996.
- Carlson, D.W., 2011. Porphyroblast crystallization: linking processes, kinetics, and microstructures. *International Geology Review*, **53**, 406–445.
- Carlson, W.D. & Johnson, C.D., 1991. Coronal reaction textures in garnet amphibolites of the Llano Uplift. *American Mineralogist*, **76**, 756–772.
- Cuthbert, S.J., Carswell, D.E.A., Krogh-Ravna, E.J. & Wain, A., 2000. Eclogites and eclogites in the Western Gneiss region, Norwegian Caledonides. *Lithos*, **52**, 165–195.
- Denison, C. & Carlson, W.D., 1997. Three-dimensional quantitative textural analysis of metamorphic rocks using high-resolution computed X-ray tomography : Part II . Application to natural samples. *Journal of Metamorphic Geology*, **15**, 45–57.
- Dobbs, H.T., Peruzzo, L., Seno, F., Spiess, R. & Prior, D.J., 2003. Unraveling the Schneeberg garnet puzzle: A numerical model of multiple nucleation and coalescence. *Contributions to Mineralogy and Petrology*, **146**, 1–9.
- Engvik, A.K., Austrheim, H. & Andersen, T.B., 2000. Structural, mineralogical and petrophysical effects on deep crustal rocks of fluid-limited polymetamorphism, Western Gneiss Region, Norway. *Journal of the Geological Society*, **157**, 121–134.
- Engvik, A.K., Austrheim, H. & Erambert, M., 2001. Interaction between fluid flow, fracturing and mineral growth during eclogitization, an example from the Sunnfjord area, Western Gneiss Region, Norway. *Lithos*, **57**, 111–141.
- Fusseis, F. & Handy, M.R., 2008. Micromechanisms of shear zone propagation at the brittle-viscous transition. *Journal of Structural Geology*, **30**, 1242–1253.
- Fusseis, F., Handy, M.R. & Schrank, C., 2006. Networking of shear zones at the brittle-to-viscous transition (Cap de Creus, NE Spain). *Journal of Structural Geology*, **28**, 1228–1243.
- Fusseis, F., Schrank, C., Liu, J., Karrech, A., Llana-Fúnez, S., Xiao, X. & Regenauer-Lieb, K., 2012. Pore formation during dehydration of a polycrystalline gypsum sample observed and quantified in a time-series synchrotron X-ray micro-tomography experiment. *Solid Earth*, **3**, 71–86.
- Getsinger, A.J. & Hirth, G., 2014. Amphibole fabric formation during diffusion creep and the rheology of shear zones. *Geology*, **42**, 535–538.
- Goergen, E.T. & Whitney, D.L., 2012. Corona networks as three-dimensional records of transport scale and pathways during metamorphism. *Geology*, **40**, 183–186.

- Hacker, B.R. & Andersen, T.B., 2010. High-temperature deformation during continental-margin subduction and exhumation: The ultrahigh-pressure Western Gneiss Region of Norway. *Tectonophysics*, **480**, 149–171.
- Hirsch, D. M., Prior, D. J. & Carlson, W., 2003. An overgrowth model to explain multiple, dispersed high-Mn regions in the cores of garnet porphyroblasts. *American Mineralogist*, **88**, 131–141.
- Ji, S. & Martignole, J., 1996. Ductility of garnet as an indicator of extremely high temperature deformation: reply. *Journal of Structural Geology*, **18**, 1375–1379.
- Ji, S. & Martignole, J., 1994. Pergamon Ductility of garnet as an indicator of extremely high temperature deformation. *Journal of Structural Geology*, **16**, 985–996.
- Jiang, D. & Williams, P.F., 2004. Reference frame, angular momentum, and porphyroblast rotation. *Journal of Structural Geology*, **26**, 2211–2224.
- John, T., Medvedev, S. & Rüpke, L.H., 2009. Generation of intermediate-depth earthquakes by self-localizing thermal runaway. *Nature Geoscience*, **2**, 137–140.
- John, T. & Schenk, V., 2003. Partial eclogitisation of gabbroic rocks in a late Precambrian subduction zone (Zambia): prograde metamorphism triggered by fluid infiltration. *Contributions to Mineralogy and Petrology*, **146**, 174–191.
- Johnson, S.E., 1993. Testing models for the development of spiral-shaped inclusion trails in garnet porphyroblasts: to rotate or not to rotate, that is the question. *Journal of Metamorphic Geology*, **11**, 635–659.
- Johnson, C.D. & Carlson, W.D., 1990. The origin of olivine-plagioclase coronas in metagabbros from the Adirondack Mountains, New York. *Journal of Metamorphic Geology*, **8**, 697–717.
- Keller, L.M., Abart, R., Stünitz, H. & De Capitani, C., 2004. Deformation, mass transfer and mineral reactions in an eclogite facies shear zone in a polymetamorphic metapelite (Monte Rosa nappe, western Alps). *Journal of Metamorphic Geology*, **22**, 97–118.
- Ketcham, R.A., 2005. Computational methods for quantitative analysis of three-dimensional features in geological specimens. *Geosphere*, **1**, 32–41.
- Ketcham, R.A. & Ryan, T.M., 2004. Quantification and visualization of anisotropy in trabecular bone. *Journal of microscopy*, **213**, 158–71.
- Konrad-Schmolke, M., Handy, M.R., Babist, J. & O'Brien, P.J., 2005. Thermodynamic modelling of diffusion-controlled garnet growth. *Contributions to Mineralogy and Petrology*, **149**, 181–195.
- Krabbendam, M. & Dewey, J.F., 1998. Exhumation of UHP rocks by transtension in the Western Gneiss Region, Scandinavian Caledonides. *Geological Society, London, Special Publications*, **135**, 159–181.
- Krabbendam, M., Wain, A. & Andersen, T.B., 2000. Pre-Caledonian granulite and gabbro enclaves in the Western Gneiss Region, Norway: indications of incomplete transition at high pressure. *Geological Magazine*, **137**, 235–255.
- Labrousse, L., Hetényi, G., Raimbourg, H., Jolivet, L. & Andersen, T.B., 2010. Initiation of crustal-scale thrusts triggered by metamorphic reactions at depth: Insights from a comparison between the Himalayas and Scandinavian Caledonides. *Tectonics*, **29**, 1–14.
- Labrousse, L., Jolivet, L., Andersen, T.B., Agard, P., Hebert, R., Maluski, H. & Scharer, U., 2004. Pressure-temperature-time deformation history of the exhumation of ultra-high pressure rocks in the Western Gneiss Region, Norway. *Geological Society of America*, **380**, 155–183.
- Lanari, P., Vidal, O., De Andrade, V., Dubacq, B., Lewin, E., Grosch, E.G. & Schwartz, S.,

2014. XMapTools: A MATLAB©-based program for electron microprobe X-ray image processing and geothermobarometry. *Computers and Geosciences*, **62**, 227–240.
- Lund, M.G. & Austrheim, H., 2003. High-pressure metamorphism and deep-crustal seismicity: evidence from contemporaneous formation of pseudotachylytes and eclogite facies coronas. *Tectonophysics*, **372**, 59–83.
- Martelat, J.E., Malamoud, K., Cordier, P., Randrianasolo, B., Schulmann, K. & Lardeaux, J.M., 2012. Garnet crystal plasticity in the continental crust, new example from south Madagascar. *Journal of Metamorphic Geology*, **30**, 435–452.
- Massey, M. A., Prior, D.J. & Moecher, D.P., 2011. Microstructure and crystallographic preferred orientation of polycrystalline microgarnet aggregates developed during progressive creep, recovery, and grain boundary sliding. *Journal of Structural Geology*, **33**, 713–730.
- Means, W.D., 1995. Shear zones and rock history. *Tectonophysics*, **247**, 157–160.
- Menegon, L., Fousseis, F., Stünitz, H. & Xiao, X., 2015. Creep cavitation bands control porosity and fluid flow in lower crustal shear zones. *Geology*, **43**, 227–230.
- Miller, C., Zanetti, A., Thoni, M. & Konzett, J., 2007. Eclogitisation of gabbroic rocks: Redistribution of trace elements and Zr in rutile thermometry in an Eo-Alpine subduction zone (Eastern Alps). *Chemical Geology*, **239**, 96–123.
- Mørk, M.B.E., 1985. A gabbro to eclogite transition on Flemsoy, Sunnmøre, Western Norway. *Chemical Geology*, **50**, 283–310.
- Mørk, M.B.E., 1986. Coronite and eclogite formation in olivine gabbro (Western Norway): reaction paths and garnet zoning. *Mineralogical Magazine*, **50**, no. September.
- Müller, S., 2013. Detailed study on microstructures and element mobility during fluid-mediated pseudomorphic gabbro-to-eclogite transformation.
- Nock, R. & Nielsen, F., 2004. Statistical Region Merging. *IEEE transactions on Pattern Analysis and Machine Intelligence*, **26**, 1452–1458.
- Padrón-Navarta, J.A., Garrido, C.J., Sánchez-Navas, A., Tommasi, A., Sánchez-Vizcaíno, V.L., Gómez-Pugnaire, M.T. & Hussain, S.S., 2008. Oriented growth of garnet by topotactic reactions and epitaxy in high-pressure, mafic garnet granulite formed by dehydration melting of metastable hornblende-gabbro (Jijal Complex, Kohistan Complex, north Pakistan). *Journal of Metamorphic Geology*, **26**, 855–870.
- Prior, D.J., Wheeler, J., Brenker, F.E., Harte, B. & Matthews, M., 2000. Crystal plasticity of natural garnet: New microstructural evidence. *Geology*, **28**, 1003–1006.
- Prior, D.J., Wheeler, J., Peruzzo, L., Spiess, R. & Storey, C., 2002. Some garnet microstructures: An illustration of the potential of orientation maps and misorientation analysis in microstructural studies. *Journal of Structural Geology*, **24**, 999–1011.
- Putnis, A. & Austrheim, H., 2010. Fluid-induced processes: metasomatism and metamorphism. *Geofluids*, **10**, 254–269.
- Putnis, A. & John, T., 2010. Replacement processes in the earth's crust. *Elements*, **6**, 159–164.
- Rivers, M.L. & Wang, Y., 2006. Recent developments in microtomography at GeoSoilEnviroCARS. *Proceedings of SPIE*, **6318**, 63180J–63180J–15.
- Schindelin, J., Arganda-Carreras, I., Frise, E., Kaynig, V., Longair, M., Pietzsch, T., Preibisch, S., Rueden, C., Saalfeld, S., Schmid, B., Tinevez, J., White, D.J., Hartenstein, V., Eliceiri, K. *et al.*, 2012. Fiji: an open-source platform for biological-image analysis. *Nature Methods*, **9**, 676–682.
- Schlüter, S., Sheppard, A., Brown, K. & Wildenschild, D., 2014. Image processing of

- multiphase images obtained via X-ray microtomography: A review. *Water Resources Research*, **50**, 3615–3639.
- Smit, M., Scherer, E.E., John, T. & Janssen, A., 2011. Creep of garnet in eclogite: Mechanisms and implications. *Earth and Planetary Science Letters*, **311**, 411–419.
- Spear, F. S., & Daniel, C. G., 2000. Diffusion control of garnet growth, Harpswell Neck, Maine, USA. *Journal of Metamorphic Geology*, **19**, 179–195.
- Spiess, R., Peruzzo, L., Prior, D.J. & Wheeler, J., 2001. Development of garnet porphyroblasts by multiple nucleation, coalescence and boundary driven rotations. *Journal of Metamorphic Geology*, **19**, 269–290.
- Storey, C.D. & Prior, D.J., 2005. Plastic deformation and recrystallization of garnet: A mechanism to facilitate diffusion creep. *Journal of Petrology*, **46**, 2593–2613.
- Terry, M.P. & Heidelbach, F., 2006. Deformation-enhanced metamorphic reactions and the rheology of high-pressure shear zones, Western Gneiss Region, Norway. *Journal of Metamorphic Geology*, **24**, 3–18.
- Terry, M.P. & Heidelbach, F., 2004. Superplasticity in garnet from eclogite facies shear zones in the Haram Gabbro, Haramsøya, Norway. *Geology*, **32**, 281.
- Trepmann, C.A. & Stöckhert, B., 2002. Cataclastic deformation of garnet: A record of synseismic loading and postseismic creep. *Journal of Structural Geology*, **24**, 1845–1856.
- Tschumperle, D. & Deriche, R., 2005. Vector-Valued Image Regularization with PDEs : A Common Framework for Different Applications. *IEEE transactions on Pattern Analysis and Machine Intelligence*, **27**, 506–517.
- Viegas, G., Menegon, L. & Archanjo, C., 2016. Brittle grain-size reduction of feldspar, phase mixing and strain localization in granitoids at mid-crustal conditions (Pernambuco shear zone, NE Brazil). *Solid Earth*, **7**, 375–396.
- Voegelé, V., Ando, J.I., Cordier, P. & Liebermann, R.C., 1998. Plastic deformation of silicate garnets. I. High-pressure experiments. *Physics of the Earth and Planetary Interiors*, **108**, 305–318.
- Wain, A., Waters, D.J. & Austrheim, H., 2001. Metastability of granulites and processes of eclogitisation in the UHP region of western Norway. *Journal of Metamorphic Geology*, **19**, 609–625.
- Wang, Z. & Ji, S., 1999. Deformation of silicate garnets: Brittle-ductile transition and its geological implications. *Canadian Mineralogist*, **37**, 525–541.
- Wayte, G.J., Worden, R.H., Rubie, D.C. & Droop, G.T.R., 1989. A TEM study of disequilibrium plagioclase breakdown at high pressure: the role of infiltrating fluid. *Contributions to Mineralogy and Petrology*, **101**, 426–437.
- Whitney, D.L., Goergen, E.T., Ketcham, R. A. & Kunze, K., 2008. Formation of garnet polycrystals during metamorphic crystallization. *Journal of Metamorphic Geology*, **26**, 365–383.
- Whitney, D.L. & Seaton, N.C.A., 2010. Garnet polycrystals and the significance of clustered crystallization. *Contributions to Mineralogy and Petrology*, **160**, 591–607.
- Zhang, J. & Green, H.W., 2007. Experimental investigation of eclogite rheology and its fabrics at high temperature and pressure. *Journal of Metamorphic Geology*, **25**, 97–115.

SUPPORTING INFORMATION

Appendix S1 Ground-truthing: Correlating synchrotron X-ray micro-tomography data with chemical compositions

Appendix S2 Segmentation of micro-tomographic data

Appendix S3 4D evolution of grain shapes

Figure S1 Grey value histograms calculated from three $S\mu$ CT datasets. The calculated absorption coefficients (μ) for the mineral phases correlate with grey scale values measured on the microtomographic data. The histograms reflect the metamorphic reactions during strain localization.

Figure S2 Schematic workflow used to analyse the microtomographic data.

Figure S3 EBSD results of low strain domain (sample 066B2). On EBSD-derived maps, high-angle boundaries (grain boundaries, misorientation $> 10^\circ$) and low-angle boundaries (subgrain boundaries, misorientation $> 3^\circ$ and $< 10^\circ$) were indicated with black and fuchsia lines, respectively. a) Phase map: Olivine (yellow), Plagioclase (white), Orthopyroxene (blue), Garnet (red), Hornblende (green). Red lines represent twinning boundaries in plagioclase. b) Inverse Pole Figure of garnet in relation to the stretching lineation in the shear zone. Legend on bottom left corner. c) Local Misorientation Map, and legend, representing local misorientations from 0 (blue) to 9 degrees misorientation (red). The arrow indicates the average local internal misorientation. d) Misorientation profile A-A', location shown in figure c).

Figure S4 EBSD results of low strain domain (sample 066B2). e) Pole figures of garnet. Equal area projections, upper hemisphere. Half width is 15° , maximum intensity is 5.54 and total number of grains is 41. f) Pole figure of hornblende. Equal area projections, upper hemisphere. Half width 15° , maximum intensities 7.91 and total number of grains is 130. g) Misorientation axis in crystal coordinates for low angle boundaries (3 - 10°).

Figure S5 EBSD results of intermediate strain domain (sample 0617). a) Inverse Pole Figure of garnet. Legend as in Fig. S3b. b) Local Misorientation Map, and legend representing local misorientations from 0 (blue) to 9 degrees misorientation (red). The arrow indicates the average local internal misorientation. c) Misorientation profile A-A', location is shown in figure a). d) Misorientation profile B-B', location shown in figure a). e) Pole figures of garnet. Equal area projections, upper hemisphere. Half width is 15° , maximum intensity 2.74 and total number of grains is 255. The trace of the shear foliation is oriented NW-SE, pole figures are oriented with the trace of the mylonitic foliation parallel to the diameter (E-W). f) Misorientation axis of low angle boundaries (3 - 10°) in crystal coordinates.

Figure S6 EBSD results of high strain domain (sample 0618). a) Phase map: Grt (red), Am (green), Opx (blue), Bt (yellow). b) Local Misorientation Map, and legend representing local misorientations from 0 (blue) to 9 degrees misorientation (red). The arrow indicates the average local internal misorientation. c) Inverse Pole Figure of garnet. Legend as in Fig. S3b. d) Misorientation profile A-A', location is shown in figure c). e) Misorientation profile B-B', location shown in figure d). f) Misorientation profile C-C', location shown in figure c).

Figure S7 EBSD results of high strain domain (sample 0618). a) Pole figures of garnet.

Equal area projections, upper hemisphere. Half width 15° , maximum intensity 1.96 and total number of grains is 223. The trace of the shear foliation is oriented NNE-SSW, pole figures are oriented with the trace of the mylonitic foliation parallel to the diameter (E-W). b) Pole figures of hornblende. Equal area projections, upper hemisphere. Half width is 15° , maximum intensity 2.04 and total number of grains is 856. c) Misorientation axis of low angle boundaries ($3\text{-}10^\circ$) in crystal coordinates.

Figure S8 The image shows the results of Statistical Region Merging technique for increasing Q. Scale as in image a). a) Original data. b) SRM Q=2. c) SRM Q=10. d) SRM Q=25: note that the image is more detailed. e, f, g) Histograms relative to the three different SRM parameters.

Figure S9 Label analysis of intermediate strain domain after erosion. The large interconnected voxel cluster is now divided in disconnected subvoxel clusters. Long side $2630\ \mu\text{m}$.

Figure S10 Quant3D explained. The tomographic data are first segmented to extrapolate the material of interest. Star points are placed within the segmented material: the distance of each star points to the next material boundary are calculated in many orientations and normalised. Simplified from Ketcham (2005).

Figure S11 Results of Quant3D analysis on eroded data, from low strain (a) to high strain (c). With increasing deformation, garnet grains evolve from isodiametric shapes to more progressively discoid shapes as a results of the deformation.

Figure S12 Histograms of GB cutoff misorientation (MO) angles: a) Low strain, b) Intermediate strain, c) High strain. The histograms confirmed that the vast majority of boundaries are indeed characterized by misorientation angles < 10 degrees- there has to be a sharp cutoff at 10 degrees, thus lending further support to the choice of using 10 degrees as threshold between low- and high-angle boundaries.

Table S1 Electron microprobe chemical compositions of oxides in garnets, used to calculate the X-ray absorption coefficients.

Table S2 Representative garnet structural formulae for the low (#066B2) and high (#0618) strain domain obtained from the microprobe analyses at the University of Münster.

Table S3 Frequency distribution data for non-eroded data. The first column of each dataset refers to absolute frequency, the second one to the cumulative frequency relative to the total amount of garnet in each sample.

Table S4 Frequency distribution data for eroded data. Bins refer to cubic micrometres. The first column of each dataset refers to absolute frequency, the second one to the cumulative frequency relative to the total amount of garnet in each sample.

FIGURE CAPTIONS

Figure 1 The illustration shows the approximate original position (circles) of thin sections in the hand specimen, and the positions of tomographic data in the thin sections which are indicated by the red squares. 3D volume renderings, derived from tomographic data from the three samples, are shown in the bottom part. Slice is cut parallel to the fabric attractor. Axis for the kinematic frame (X, Y, Z) are indicated in the microtomographic data.

Figure 2 Microtomographic datasets: a) low strain, b) intermediate strain, and c) high strain. Figure a) exhibits minor artefacts (horizontal stripes) that do not affect the analyses. Mineral phases and features are recognizable from the corresponding SEM images (Fig. 3). The images represent the XZ plane and are parallel to the thin sections.

Figure 3 BSE images of Krakeneset samples and corresponding microtomographic datasets, from low to high strain domain respectively: a) Sample 066B2 (Low strain)- Olivine grains are surrounded by complex coronas of orthopyroxene, garnet and amphibole. b) 3-dimensional dataset of low strain domain: high-pressure amphibole-garnet coronas surround olivine grains (dimensions 1503 x 1196 x 1831 cubic voxels). Note the variable thickness of amphibole. c) Sample 0617 (Intermediate Strain)- In the intermediate strain domain, olivine cores are replaced by orthopyroxene, while garnet and amphibole are no more part of the corona structures. d) Corresponding microtomographic dataset (dimensions 1322 x 1219 x 2023 cubic voxels). e) Sample 0618 (High Strain)- The high strain domain is characterized by a compositional layering of elongated garnet and plagioclase versus orthopyroxene and amphibole rich layers. f) Microtomographic dataset of the high strain domain (dimensions 1313 x 1234 x 1980 cubic voxels): note garnet grains behaving as rigid objects in a more ductile matrix of orthopyroxene and amphibole.

Figure 4 a) Optical microscope image illustrating the mineral phases and microstructures present in the more deformed samples. b) BSE image showing old olivine cores now replaced by orthopyroxene-amphibole symplectites. Relict cores of magmatic clinopyroxene are present (Mag_Cpx “relict”), and are surrounded by a thin rim of omphacite (Omp), which is present also between garnet and orthopyroxene-amphibole symplectites (“Opx-Amp Symp”). c) Symplectites of albite-clinzoisite are replacing the plagioclase; omphacite surrounds relict magmatic clinopyroxene (Mag_Cpx “relict”) and orthopyroxene-amphibole symplectites.

Figure 5 Grs-Alm-Py plot showing garnet compositions from EMPA analyses, as single measurements across different grains. End-members values, calculated as average from the single measurements, are presented in the graph by the large symbols. Filled symbols represent compositions compositionally closer to the plagioclase source (richer in CaO). Empty symbols represent compositions richer in Fe-Mg. With increasing deformation, garnet compositions become more Alm-rich, a trend expected for a gabbro that is equilibrating under P-T-t conditions of eclogite facies. In Tab. S2, representative structural formulae are reported for the three samples.

Figure 6 Compositional maps for CaO and MgO for the low (a-b) and high (c-d) strain domains, obtained using XMapTools v. 2.3.1 (Lanari *et al.*, 2014). CaO and MgO do have the same compositional zoning (4-10%) in the most deformed sample. C) Many garnets in the high strain domain have low CaO, reflecting an equilibration towards Alm-rich compositions.

The higher content in CaO (~10%) (a') and MgO (~11%) (b') shown by some grain is interpreted as to result from coalescence (a, b) and subsequent disintegration of individual zoned coronas. Fine-grained garnets (Fig. 6c to the left) represent highly fragmented and collapsed former coronas.

Figure 7 The figures illustrate the results of segmentation of garnet from the microtomographic data. Top: cropped volumes of original datasets (~0.5 mm³); bottom: garnets rendered in purple. Fog is added within the datasets to better visualize the 3D architecture. a) Low strain, b) Intermediate strain, c) High strain. Note 3D orientation and texture of garnet grains. Note the presence of more faceted grains in the intermediate and high strain domain.

Figure 8 Garnet voxel cluster size distribution for non-eroded (solid lines) and eroded (dashed lines) data. From low to high strain, there is an increase in frequency for all size classes with increasing strain. Note the presence of the very large interconnected garnet voxel cluster in the low strain domain (blue solid curve), while the presence of much smaller sizes in the most deformed sample. The sketch on the top left corner illustrates the erosion process and the effects of particle size and shape: some particle might completely disappear. a,b) Absolute frequency and cumulative volume, respectively, for the low strain sample. c, d) Absolute frequency and cumulative volume, respectively, for the intermediate strain sample. e, f) Absolute frequency and cumulative volume, respectively, for the high strain sample.

Figure 9 Label analysis of the end-members of the studied samples. a) 3D volume rendering of labels relative to low strain domain (dimensions 1503 x 1196 x 1831 cubic voxels). b) Intermediate Strain (dimensions 1322 x 1219 x 2023 cubic voxels). c) High strain (dimensions 1313 x 1234 x 1980 cubic voxels). Individual disconnected aggregates of garnet are identified with different colours.

Figure 10 Outputs of segmentation for olivine (green) and garnet (blue) grains, in the low strain domain (different viewing angles). The red arrows indicate olivine grains that are not completely enclosed by garnet coronas.

Figure 11 EBSD analysis results. Low strain: a) IPF map superposed on a pattern quality (Band Contrast) map. b) Profile X-Y, location in figure a). c) Misorientation axis by crystal coordinates for low angle boundaries (3-10°). Intermediate strain domain: d) IPF map. e) Profile X-Y, location in figure d; f) Misorientation axis by crystal coordinates for low angle boundaries (3-10°). High strain: g) IPF map. h) Profile X-Y, location in figure g; i) Misorientation axis by crystal coordinates for low angle boundaries (3-10°).

Figure 12 Schematic sketch illustrating the evolution of reaction microfabrics, and in particular of garnet grains. a) Low strain domain. b) Intermediate strain. c) High strain. See text for discussion.

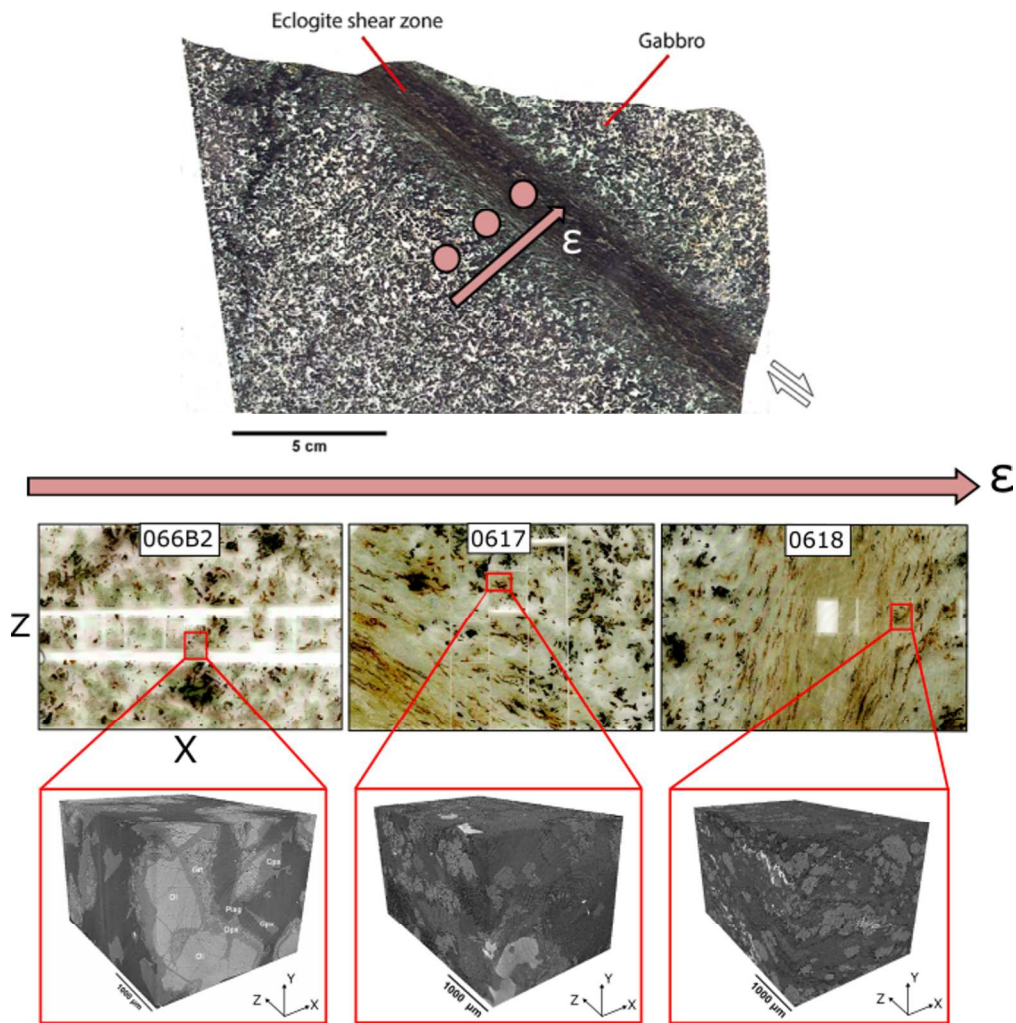


Figure 1

150x152mm (300 x 300 DPI)

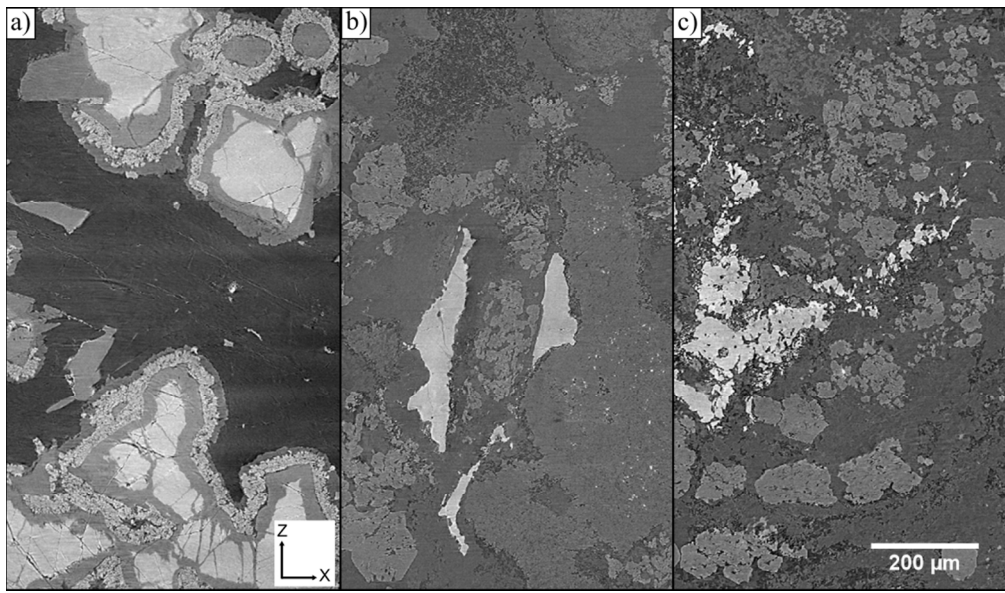


Figure 2

150x87mm (300 x 300 DPI)

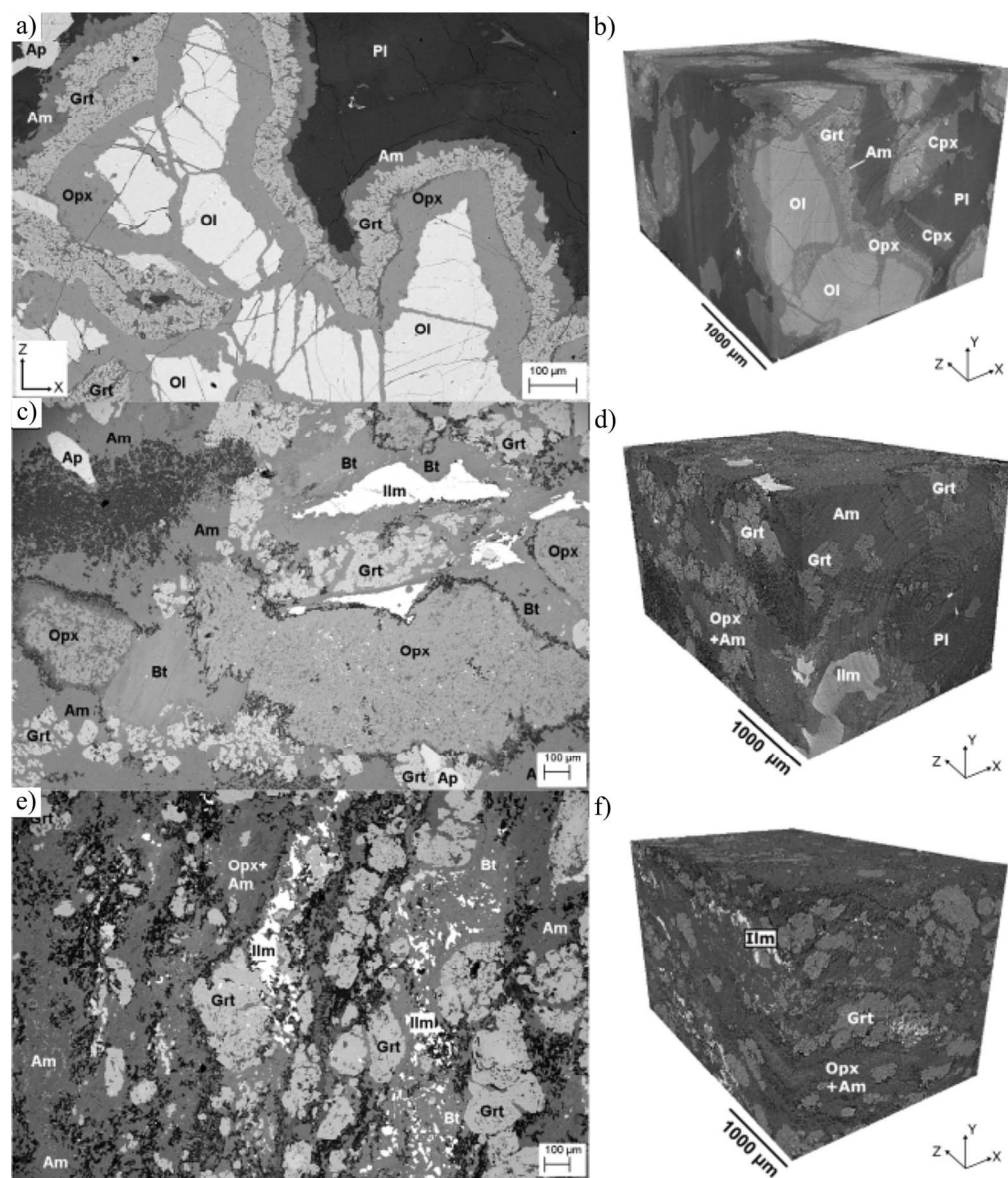


Figure 3

150x175mm (300 x 300 DPI)

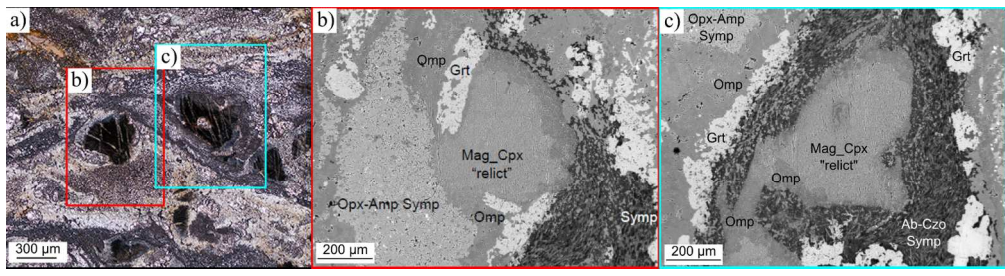


Figure 4

150x39mm (300 x 300 DPI)

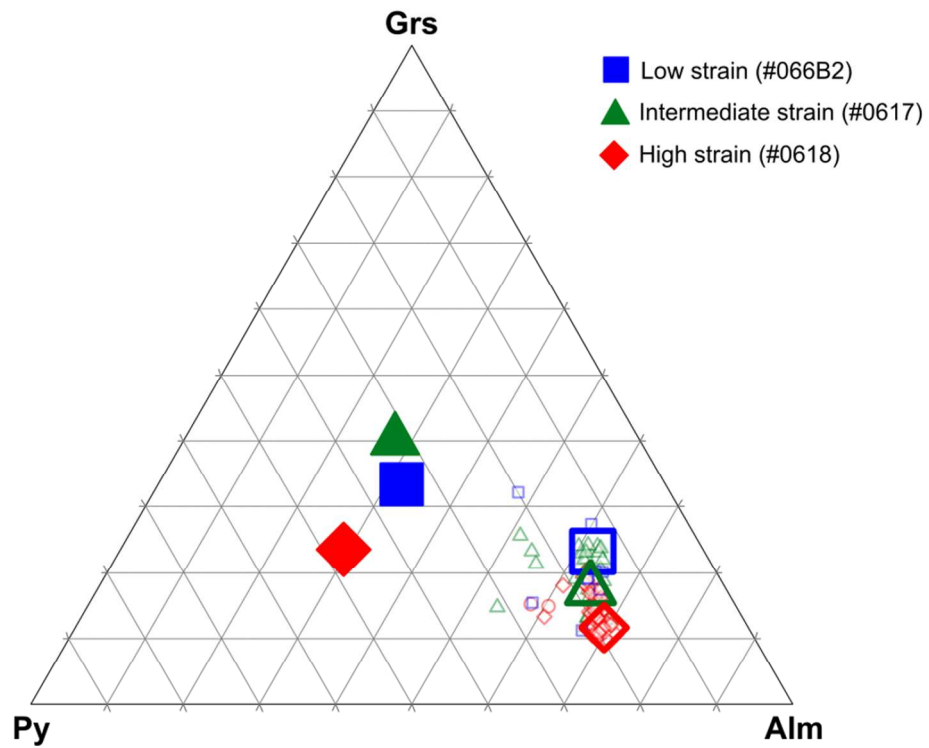


Figure 5

99x75mm (300 x 300 DPI)

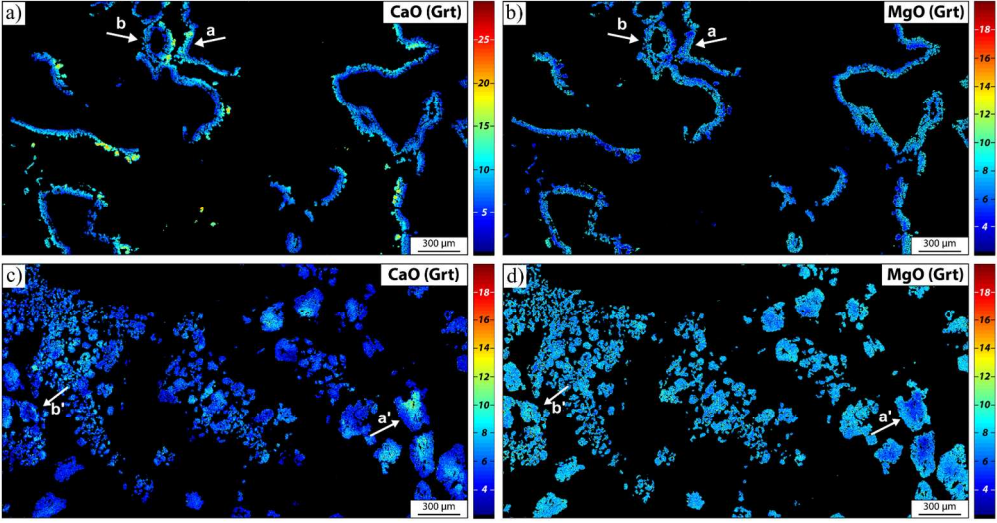


Figure 6

150x78mm (300 x 300 DPI)

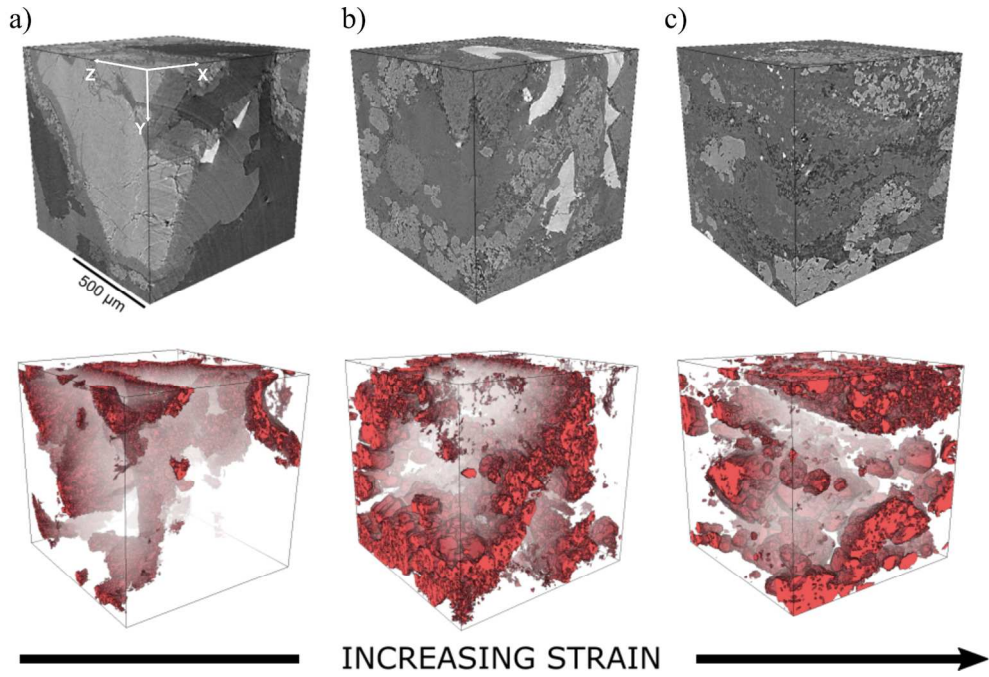


Figure 7

150x99mm (300 x 300 DPI)

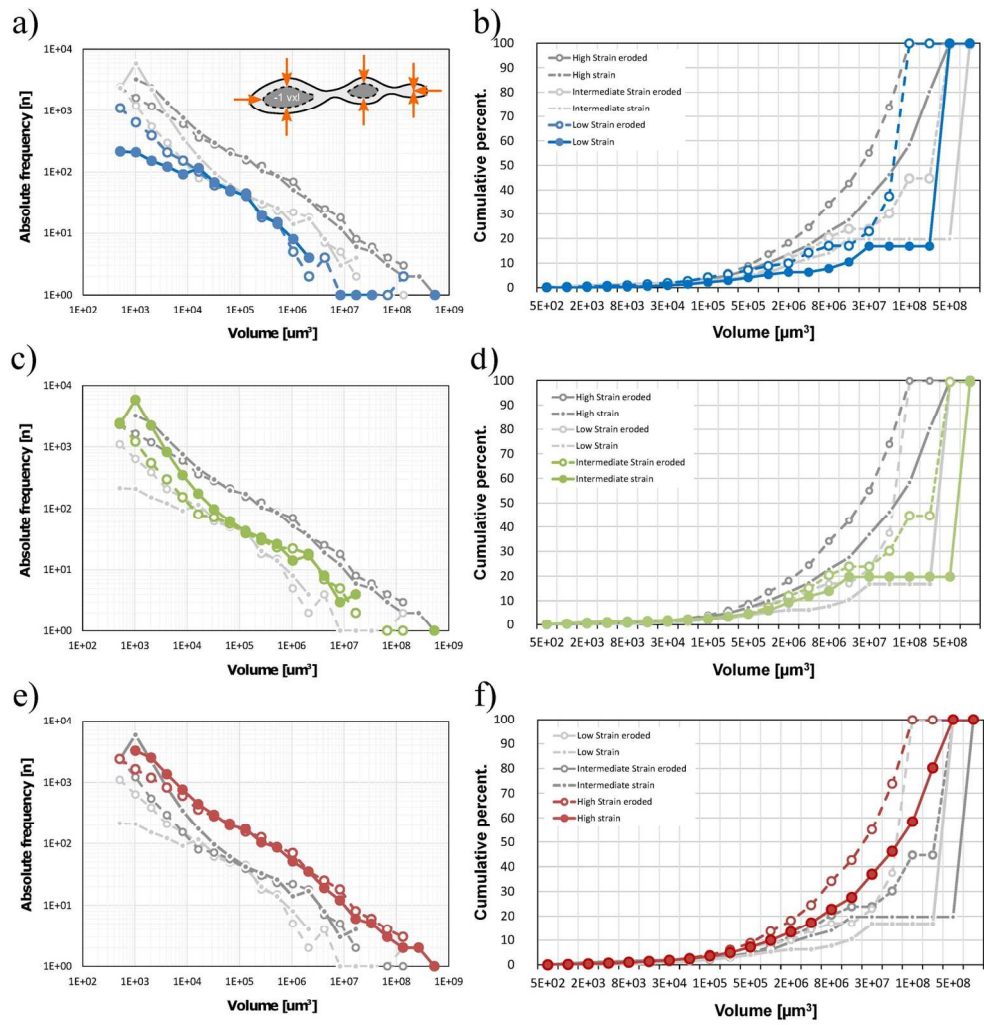


Figure 8

153x155mm (300 x 300 DPI)

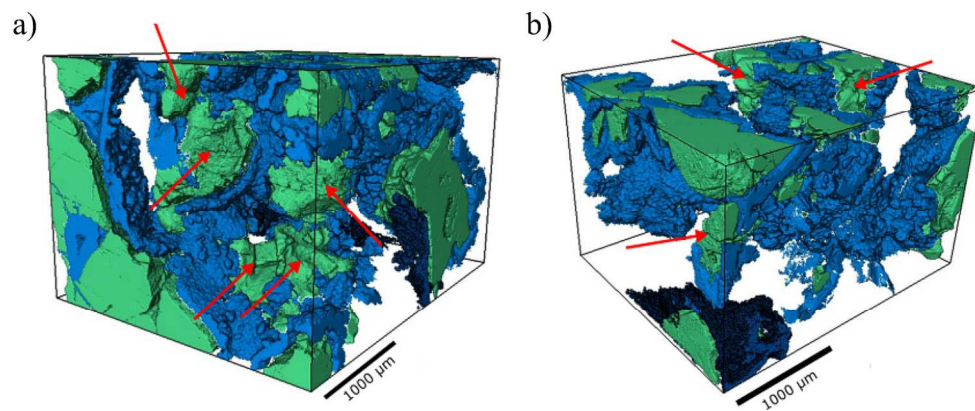


Figure 9

150x59mm (300 x 300 DPI)

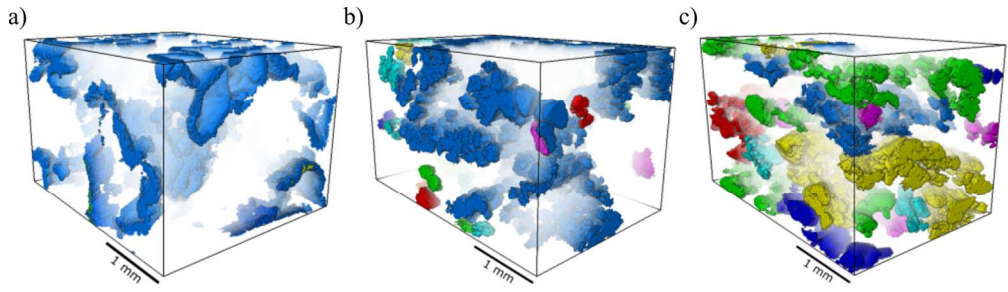


Figure 10

150x41mm (300 x 300 DPI)

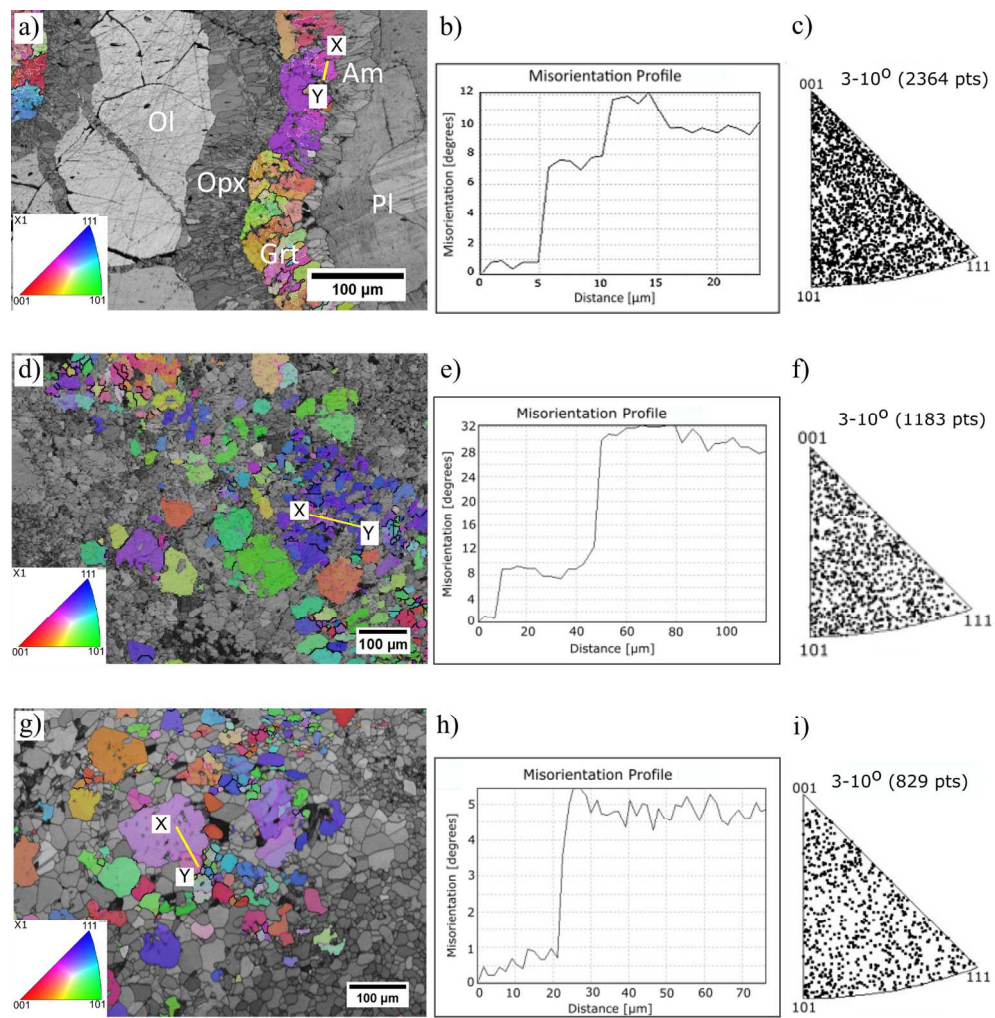


Figure 11

150x151mm (300 x 300 DPI)

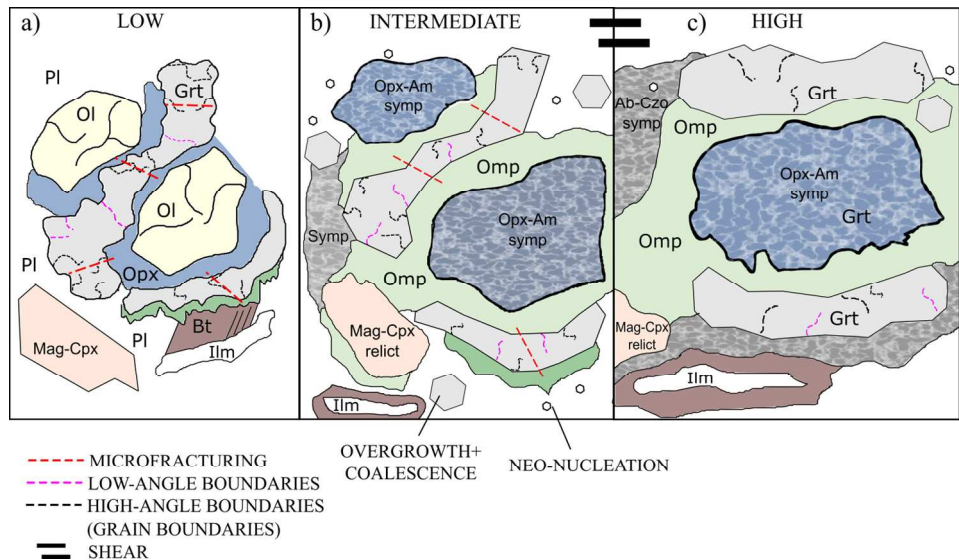


Figure 12

150x82mm (300 x 300 DPI)

The strain-dependent spatial evolution of garnet in a high-pressure ductile shear zone from the Western Gneiss Region (Norway): a synchrotron X-ray microtomography study

A. Macente^{1*}, F. Füsseis¹, L. Menegon², X. Xianghui³, T. John⁴

¹ School of Geosciences, The King's Building, James Hutton Road, Edinburgh, EH9 3FE

² School of Geography, Earth and Environmental Sciences (Faculty of Science and Engineering), Fitzroy, Drake Circus, Plymouth, Devon, PL4 8AA

³ Argonne National Laboratory, 9700 S. Cass Ave, Building 431-B003

⁴ Institut für Geologische Wissenschaften, Freie Universität Berlin, Malteserstr. 74-100, 12249 Berlin

* Corresponding author's e-mail:

alice.macente@ed.ac.uk, alice.macente@gmail.com

Short title: Strain-dependent evolution of garnet

SUPPORTING INFORMATION

Appendix S1 Ground-truthing: Correlating synchrotron X-ray micro-tomography data with chemical compositions

Appendix S2 Segmentation of micro-tomographic data

Appendix S3 4D evolution of grain shapes

Figure S1 Grey value histograms calculated from three S μ CT datasets. The calculated absorption coefficients (μ) for the mineral phases correlate with grey scale values measured on the microtomographic data. The histograms reflect the metamorphic reactions during strain localization.

Figure S2 Schematic workflow used to analyse the microtomographic data.

Figure S3 EBSD results of low strain domain (sample 066B2). On EBSD-derived maps, high-angle boundaries (grain boundaries, misorientation $> 10^\circ$) and low-angle boundaries (subgrain boundaries, misorientation $> 3^\circ$ and $< 10^\circ$) were indicated with black and fuchsia lines, respectively. a) Phase map: Olivine (yellow), Plagioclase (white), Orthopyroxene (blue), Garnet (red), Hornblende (green). Red lines represent twinning boundaries in plagioclase. b) Inverse Pole Figure of garnet in relation to the stretching lineation in the shear zone. Legend on bottom left corner. c) Local Misorientation Map, and legend, representing local misorientations from 0 (blue) to 9 degrees misorientation (red). The arrow indicates the average local internal misorientation. d) Misorientation profile A-A', location shown in

figure c).

Figure S4 EBSD results of low strain domain (sample 066B2). e) Pole figures of garnet. Equal area projections, upper hemisphere. Half width is 15° , maximum intensity is 5.54 and total number of grains is 41. f) Pole figure of hornblende. Equal area projections, upper hemisphere. Half width 15° , maximum intensities 7.91 and total number of grains is 130. g) Misorientation axis in crystal coordinates for low angle boundaries ($3\text{-}10^\circ$).

Figure S5 EBSD results of intermediate strain domain (sample 0617). a) Inverse Pole Figure of garnet. Legend as in Fig. S3b. b) Local Misorientation Map, and legend representing local misorientations from 0 (blue) to 9 degrees misorientation (red). The arrow indicates the average local internal misorientation. c) Misorientation profile A-A', location is shown in figure a). d) Misorientation profile B-B', location shown in figure a). e) Pole figures of garnet. Equal area projections, upper hemisphere. Half width is 15° , maximum intensity 2.74 and total number of grains is 255. The trace of the shear foliation is oriented NW-SE, pole figures are oriented with the trace of the mylonitic foliation parallel to the diameter (E-W). f) Misorientation axis of low angle boundaries ($3\text{-}10^\circ$) in crystal coordinates.

Figure S6 EBSD results of high strain domain (sample 0618). a) Phase map: Grt (red), Am (green), Opx (blue), Bt (yellow). b) Local Misorientation Map, and legend representing local misorientations from 0 (blue) to 9 degrees misorientation (red). The arrow indicates the average local internal misorientation. c) Inverse Pole Figure of garnet. Legend as in Fig. S3b. d) Misorientation profile A-A', location is shown in figure c). e) Misorientation profile B-B', location shown in figure d). f) Misorientation profile C-C', location shown in figure c).

Figure S7 EBSD results of high strain domain (sample 0618). a) Pole figures of garnet. Equal area projections, upper hemisphere. Half width 15° , maximum intensity 1.96 and total number of grains is 223. The trace of the shear foliation is oriented NNE-SSW, pole figures are oriented with the trace of the mylonitic foliation parallel to the diameter (E-W). b) Pole figures of hornblende. Equal area projections, upper hemisphere. Half width is 15° , maximum intensity 2.04 and total number of grains is 856. c) Misorientation axis of low angle boundaries ($3\text{-}10^\circ$) in crystal coordinates.

Figure S8 The image shows the results of Statistical Region Merging technique for increasing Q. Scale as in image a). a) Original data. b) SRM Q=2. c) SRM Q=10. d) SRM Q=25: note that the image is more detailed. e, f, g) Histograms relative to the three different SRM parameters.

Figure S9 Label analysis of intermediate strain domain after erosion. The large interconnected voxel cluster is now divided in disconnected subvoxel clusters. Long side $2630\ \mu\text{m}$.

Figure S10 Quant3D explained. The tomographic data are first segmented to extrapolate the material of interest. Star points are placed within the segmented material: the distance of each star points to the next material boundary are calculated in many orientations and normalised. Simplified from Ketcham (2005).

Figure S11 Results of Quant3D analysis on eroded data, from low strain (a) to high strain

(c). With increasing deformation, garnet grains evolve from isodiametric shapes to more progressively discoid shapes as a result of the deformation.

Figure S12 Histograms of GB cutoff misorientation (MO) angles: a) Low strain, b) Intermediate strain, c) High strain. The histograms confirmed that the vast majority of boundaries are indeed characterized by misorientation angles < 10 degrees- there has to be a sharp cutoff at 10 degrees, thus lending further support to the choice of using 10 degrees as threshold between low- and high-angle boundaries.

Table S1 Electron microprobe chemical compositions of oxides in garnets, used to calculate the X-ray absorption coefficients.

Table S2 Representative garnet structural formulae for the low (#066B2) and high (#0618) strain domain obtained from the microprobe analyses at the University of Münster.

Table S3 Frequency distribution data for non-eroded data. The first column of each dataset refers to absolute frequency, the second one to the cumulative frequency relative to the total amount of garnet in each sample.

Table S4 Frequency distribution data for eroded data. Bins refer to cubic micrometres. The first column of each dataset refers to absolute frequency, the second one to the cumulative frequency relative to the total amount of garnet in each sample.

Appendix S1 Ground-truthing: Correlating synchrotron X-ray micro-tomography data with chemical compositions

Where X-ray microtomographic data allow for a complete visualisation of microfabrics in rocks in 3D (Denison and Carlson, 1997; Gualda and Rivers, 2006; Whitney et al., 2008; Wang et al., 2011; Goergen and Whitney, 2012; Sayab et al., 2014), the combination with established microanalytical techniques critically expands our insight into tectonic and metamorphic processes. High-resolution microtomographic data and electron microscopic analyses have similar resolutions on the μm -scale, and analytical results from the same samples can therefore be extrapolated between the techniques. The obvious gain from this is that metamorphic microfabrics can then be fully quantified in 3D. However, the marriage of 2D with 3D analyses hinges on a) a registration of the 2D data within the 3D dataset, b) a correlation of actual compositional data from the mineral phases with intensities recorded in the 3D scalar fields that make a microtomographic dataset (Gualda and Rivers, 2006) and c) the involved procedure of segmenting individual mineral volumes from the 3-dimensional datasets to allow for a further quantitative analysis. While routines for image registration are readily available, also in *AvizoFire*[®], and segmentation is discussed in section “Image Processing and Analysis”, the following summarises our strategy to correlate X-ray absorption with compositional information.

In most microtomographic data material-specific X-ray absorption is recorded as a function of position in the sample and, as an output of the reconstruction process, stored in an array of intensity values. The relationship between absorption and intensity (usually visualised as

grey scale values) in the tomographic data is given by the Lambert-Beer law:

$$I = I_0 \exp \left[- \int_{-\infty}^{\infty} \mu(x) dx \right]$$

where I represents the intensity of the X-ray source before it hits the sample, I_0 is the attenuated intensity after X-rays passed through a sample of thickness x , and μ is a linear attenuation coefficient (e.g., Baker *et al.*, 2012; Füsseis *et al.*, 2014). The intensity distribution in a polymineralic sample can be plotted in a histogram that relates voxel frequency to recorded intensity (e.g., Fig. S1). Given that intensity is material-specific, these data can, in the best of cases, be used to quantify the volume of a particular mineral phase. However, it is important at this stage to establish a tight link between X-ray absorption microtomographic and actual compositional data from the same sample, and confirm that the grey values correspond to the minerals of interest. To achieve this we calculated the X-ray absorption coefficients for each mineral phase based on the chemical compositions acquired through EMPA analysis, and compared them with the grey scale distribution in the tomographic data (Fig. S1). X-ray mass attenuation coefficients are listed in a NIST (National Institute of Standards and Technology) database for elements $Z=1$ to 92, and for a number of substances of radiological interest. Where the energy of the incoming photons is known (in our case 27 KeV) and compositional data are available, the absorption coefficients can be calculated for any mineral. We used averaged electron microprobe analyses (EMPA) to calculate the theoretical X-ray mass attenuation coefficients of the minerals in our samples. Fig. S1 compares the calculated absorptions with three grey value histograms from the three studied datasets. Our analytical strategy, where the actual microtomography sample was polished and used for electron microscopy and EMPA analyses, allowed to combine compositional measurements with intensity signals and thereby anchor the two x-axes against each other. Fig. S1 does indeed capture some of the metamorphic processes that affect the samples. For example the peak for plagioclase, which is clearly present in the low strain dataset, is replaced by a minimum in the high strain domain, reflecting the lack (or a very small presence) of plagioclase in the eclogitic shear zone centre.

Appendix S2 Segmentation of micro-tomographic data

To be able to segment garnets from the tomographic images, we denoised the images in Fiji. The parameters for Anisotropic Diffusion Filter in 2D included 20 iterations, a_1 and a_2 were set up at 0.7 and 0.5 respectively. Before applying the filter, we improved the contrast on the images and saved them in Bitmap format in order to preserve the new contrast.

On the filtered data, Statistical Region Merging (SRM) technique was applied (Nock and Nielsen, 2004). This algorithm is a region growing technique, which groups homogeneous pixels together and grow them iteratively together by merging other pixels or smaller regions. The limit of regions to be merged together is determined by a statistical test and the scale is controlled by the size of the parameter Q : the higher is Q , the higher is the number of subregions and the more detailed is the resulting image but it is also noisier (Nock and Nielsen, 2004) (Fig. S8). The changes operated by SRM can be visualised in the image histograms. Each boundary phase is marked in the histogram by a vertical bar, which allows *Global Threshold* to segment the material of interest in a more controlled way (Fig. S8). Global thresholding allows to select from the grey scale values in the histogram, and

therefore from their X-ray absorption coefficient, a particular phase that can be extrapolated from the contest. In some cases, the choice of using one single output of SRM was insufficient. In Fiji, it was thus possible to combine different SRM outputs to obtain the best segmentation for garnet grains by using *Image Calculator* and the *Multiply* operator to get rid of unwanted segmented phases or islands.

A summary of the workflow used to analyse the data is shown in Figure S2.

Appendix S3 4D evolution of grain shapes

We performed Quant3D analysis to investigate the 3-dimensional shape of garnet grains and to understand if synchrotron X-ray micro-tomography can be used to gain information on the dynamic evolution of grain shapes. Quant3D is a fabric analysis software developed by Ketcham and Ryan (2004) and Ketcham (2005), written in IDL programming language and it includes three main fabric analysis methods. Originally developed by previous works for two-dimensional analysis (Ketcham (2005b) and references therein), these methods can now be used also to analyse 3-dimensional structures. The software gives the eigenvectors (\hat{u}_1 , \hat{u}_2 , \hat{u}_3) and eigenvalues (τ^1 , τ^2 , τ^3) of the fabric tensors, which define orthogonal principal axes and are related to the moment of inertia, the degree of anisotropies (DA), the isotropy index I and the elongation index (E) (Ketcham, 2005). The results can be visualized as a 3-dimensional rose diagram. In the rose diagram, each vertex is projected from the unit sphere either inward or outward from the origin of the star points. The vertex positions from the origin are normalized by the maximum distance value. In the rose diagram, eigenvectors, scaled by their respective eigenvalues, are also plotted. The rose diagram can be visualized as rendered surface with a colour code mode, where the red colour represents a normalized value of 1.0, as a distance from the origin equal to the coordinate axis length: lower values, indicating closer distances to the origin, are represented with cooler rainbow colours (Ketcham and Ryan (2004)). The results can be exported as VRML format, containing all the spatial information and readable by lots of applications. In our analysis, star points were placed outside the material of interest by assigning black values (0) to the garnets. In this way, the distances to the next material boundary represent distances to the material of interest, and thus they give an indication of the grain shapes. Analysis parameters were as followed: uniform distribution of orientations (513), random rotation, dense vectors. The results were exported as rose diagrams and VRML format files. In order to avoid errors introduced by image segmentation, the analysis were performed on eroded data, as previously mentioned (section "Image Processing and Analysis"). The results are shown in Fig. S12. With increasing strain, garnet shapes evolve from an isodiametric grain to increasingly discoidal and oblate shapes.

REFERENCES

- Baker, D. R., Mancini, L., Polacci, M., Higgins, M. D., Gualda, G. A. R., Hill, R. J. & Rivers, M., 2012. An introduction to the application of X-ray microtomography to the three-dimensional study of igneous rocks. *Lithos*, **148**, 262–276
- Denison, C. & Carlson, W. D., 1997. Three-dimensional quantitative textural analysis of metamorphic rocks using high-resolution computed X-ray tomography : Part II. Application to natural samples. *Journal of Metamorphic Geology*, **15**, 45–57.
- Fusseis, F., Xiao, X., Schrank, C. & De Carlo, F., 2014. A brief guide to synchrotron

- radiation-based microtomography in (structural) geology and rock mechanics. *Journal of Structural Geology*, **65**, 1–16.
- Goergen, E. T. & Whitney, D. L., 2012. Corona networks as three-dimensional records of transport scale and pathways during metamorphism. *Geology*, **40**, 183–186.
- Gualda, G. A. R. & Rivers, M., 2006. Quantitative 3D petrography using x-ray tomography: Application to Bishop Tuff pumice clasts. *Journal of Volcanology and Geothermal Research*, **154**, 48–62.
- Ketcham, R. A., 2005. Three-dimensional grain fabric measurements using high-resolution X-ray computed tomography. *Journal of Structural Geology*, **27**, 1217–1228.
- Ketcham, R. A. & Ryan, T. M., 2004. Quantification and visualization of anisotropy in trabecular bone. *Journal of microscopy*, **213**, 158–71.
- Nock, R. & Nielsen, F., 2004. Statistical Region Merging. *IEEE transactions on Pattern Analysis and Machine Intelligence*, **26**, 1452–1458.
- Sayab, M., Suuronen, J., Holtta, P., Aerden, D., Lahtinen, R. & Kallonen, A. P., 2014. High-resolution X-ray computed microtomography: A holistic approach to metamorphic fabric analyses. *Geology*, **43**, 55–58.
- Wang, W., Kravchenko, A. N., Smucker, A. J. M. & Rivers, M., 2011. Comparison of image segmentation methods in simulated 2D and 3D microtomographic images of soil aggregates. *Geoderma*, **162**, 231–241.
- Whitney, D. L., Goergen, E. T., Ketcham, R. A. & Kunze, K., 2008. Formation of garnet polycrystals during metamorphic crystallization. *Journal of Metamorphic Geology*, **26**, 365–383.

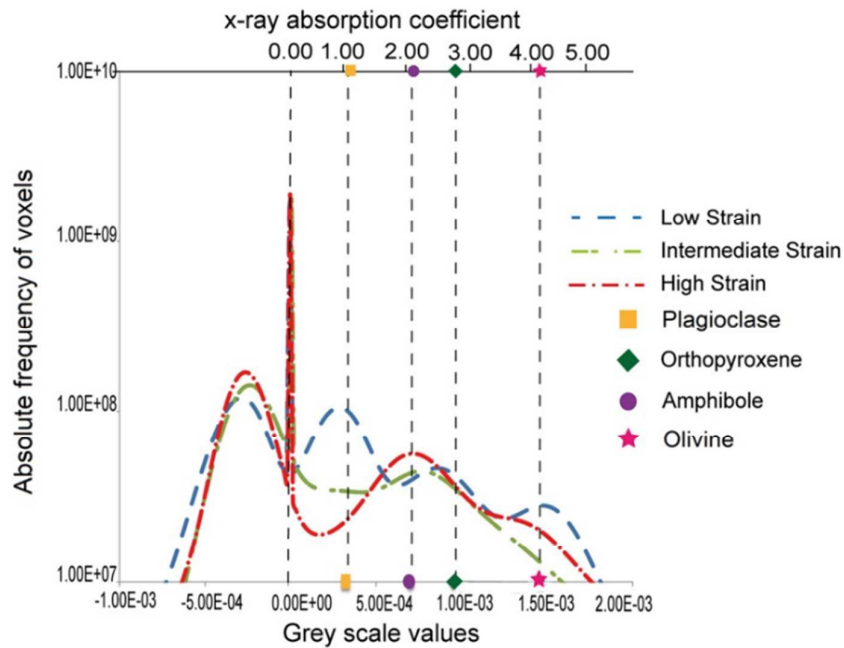


Figure S1 The graph shows grey value histograms calculated from three S μ CT datasets. The calculated absorption coefficients (μ) for the mineral phases correlate with grey scale values measured on the microtomographic data. The histograms reflect the metamorphic reactions during strain localization.

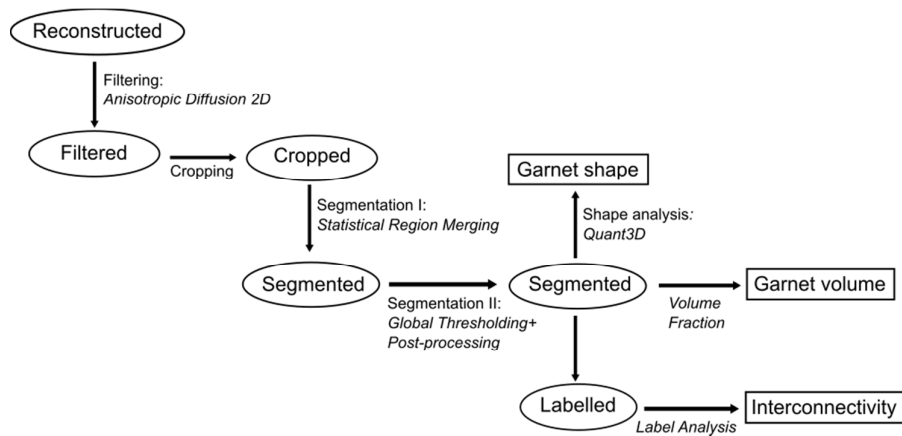


Figure S2 Schematic workflow used to analyse the microtomographic data.

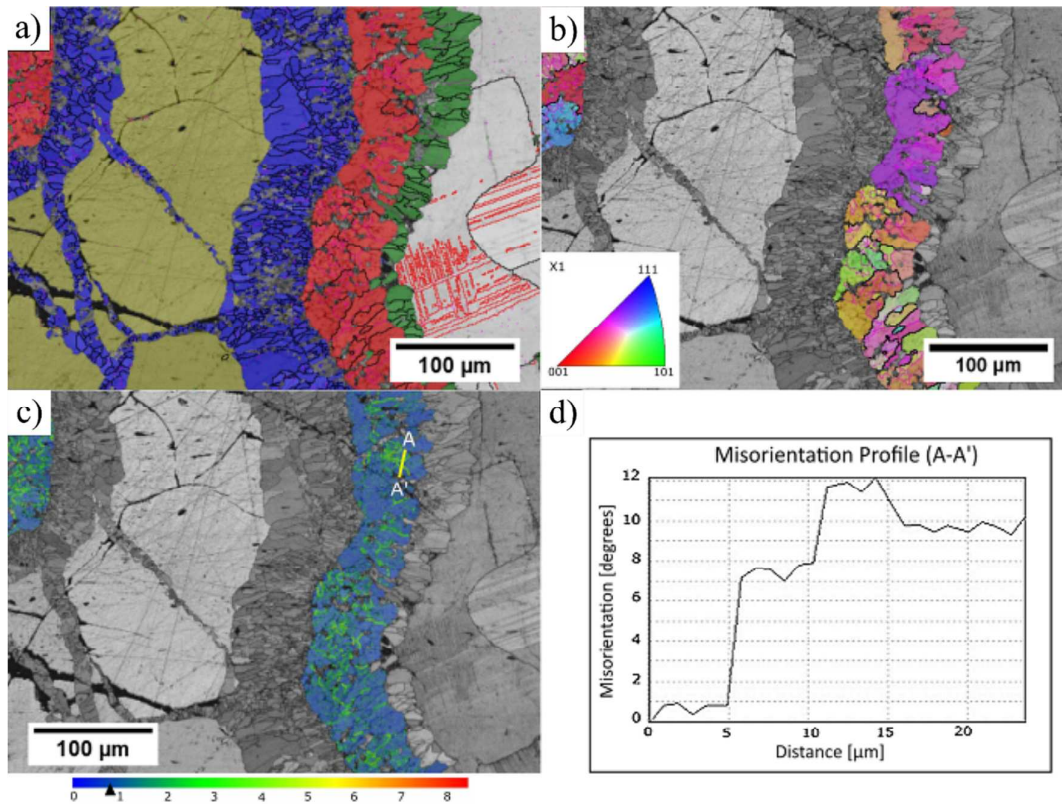


Figure S3 EBSD results of low strain domain (sample 066B2). On EBSD-derived maps, high-angle boundaries (grain boundaries, misorientation $> 10^\circ$) and low-angle boundaries (subgrain boundaries, misorientation $> 3^\circ$ and $< 10^\circ$) were indicated with black and fuchsia lines, respectively. a) Phase map: Olivine (yellow), Plagioclase (white), Orthopyroxene (blue), Garnet (red), Hornblende (green). Red lines represent twinning boundaries in plagioclase. b) Inverse Pole Figure of garnet in relation to the stretching lineation in the shear zone. Legend on bottom left corner. c) Local Misorientation Map, and legend, representing local misorientations from 0 (blue) to 9 degrees misorientation (red). The arrow indicates the average local internal misorientation. d) Misorientation profile A-A', location shown in figure c).

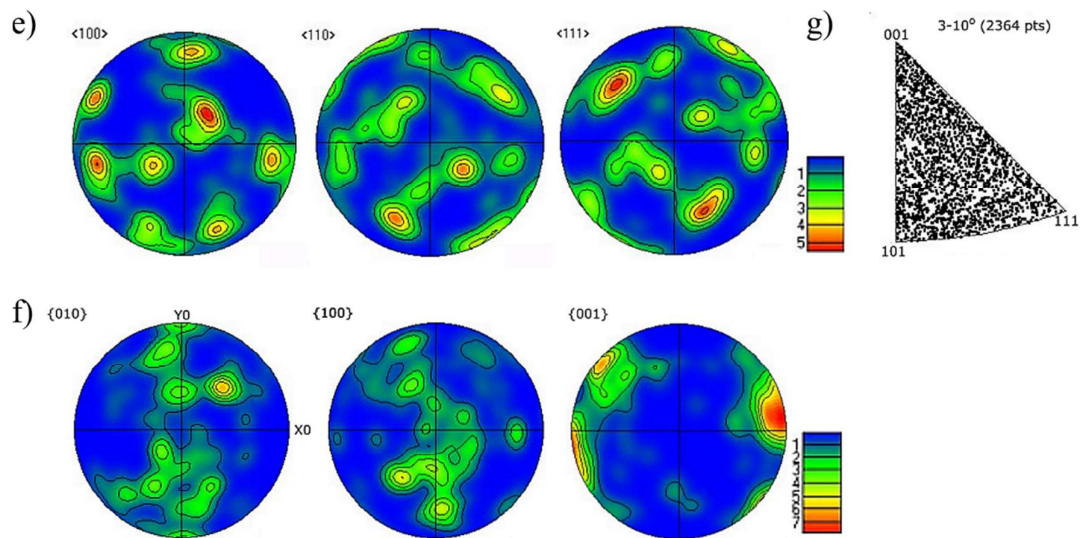


Figure S4 EBSD results of low strain domain (sample 066B2). e) Pole figures of garnet. Equal area projections, upper hemisphere. Half width is 15° , maximum intensity is 5.54 and total number of grains is 41. f) Pole figure of hornblende. Equal area projections, upper hemisphere. Half width 15° , maximum intensities 7.91 and total number of grains is 130. g) Misorientation axis in crystal coordinates for low angle boundaries ($3-10^\circ$).

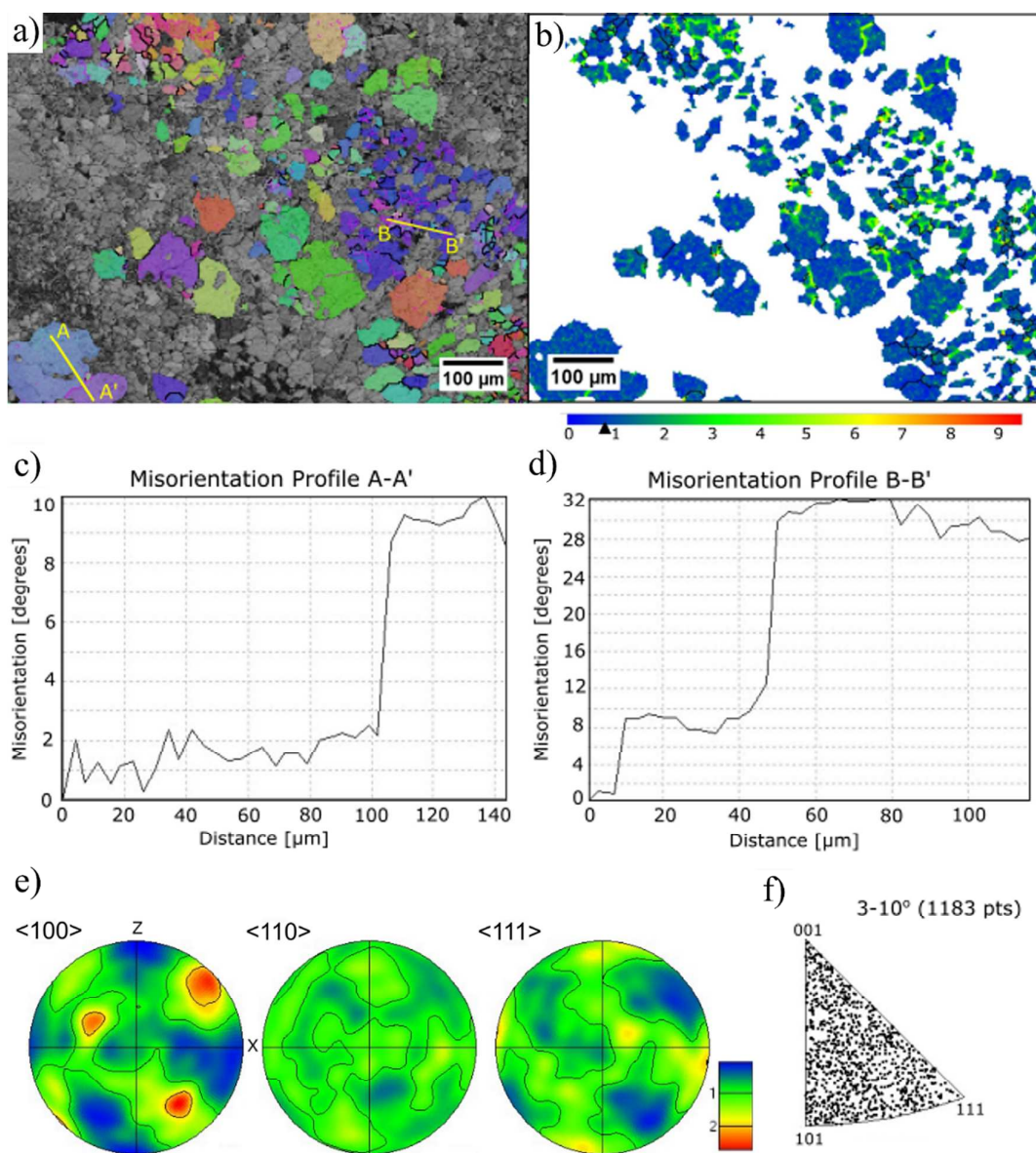


Figure S5 EBSD results of intermediate strain domain (sample 0617). a) Inverse Pole Figure of garnet. Legend as in Fig. S3b. b) Local Misorientation Map, and legend representing local misorientations from 0 (blue) to 9 degrees misorientation (red). The arrow indicates the average local internal misorientation. c) Misorientation profile A-A', location is shown in figure a). d) Misorientation profile B-B', location shown in figure a). e) Pole figures of garnet. Equal area projections, upper hemisphere. Half width is 15° , maximum intensity 2.74 and total number of grains is 255. The trace of the shear foliation is oriented NW-SE, pole figures are oriented with the trace of the mylonitic foliation parallel to the diameter (E-W). f) Misorientation axis of low angle boundaries ($3-10^\circ$) in crystal coordinates.

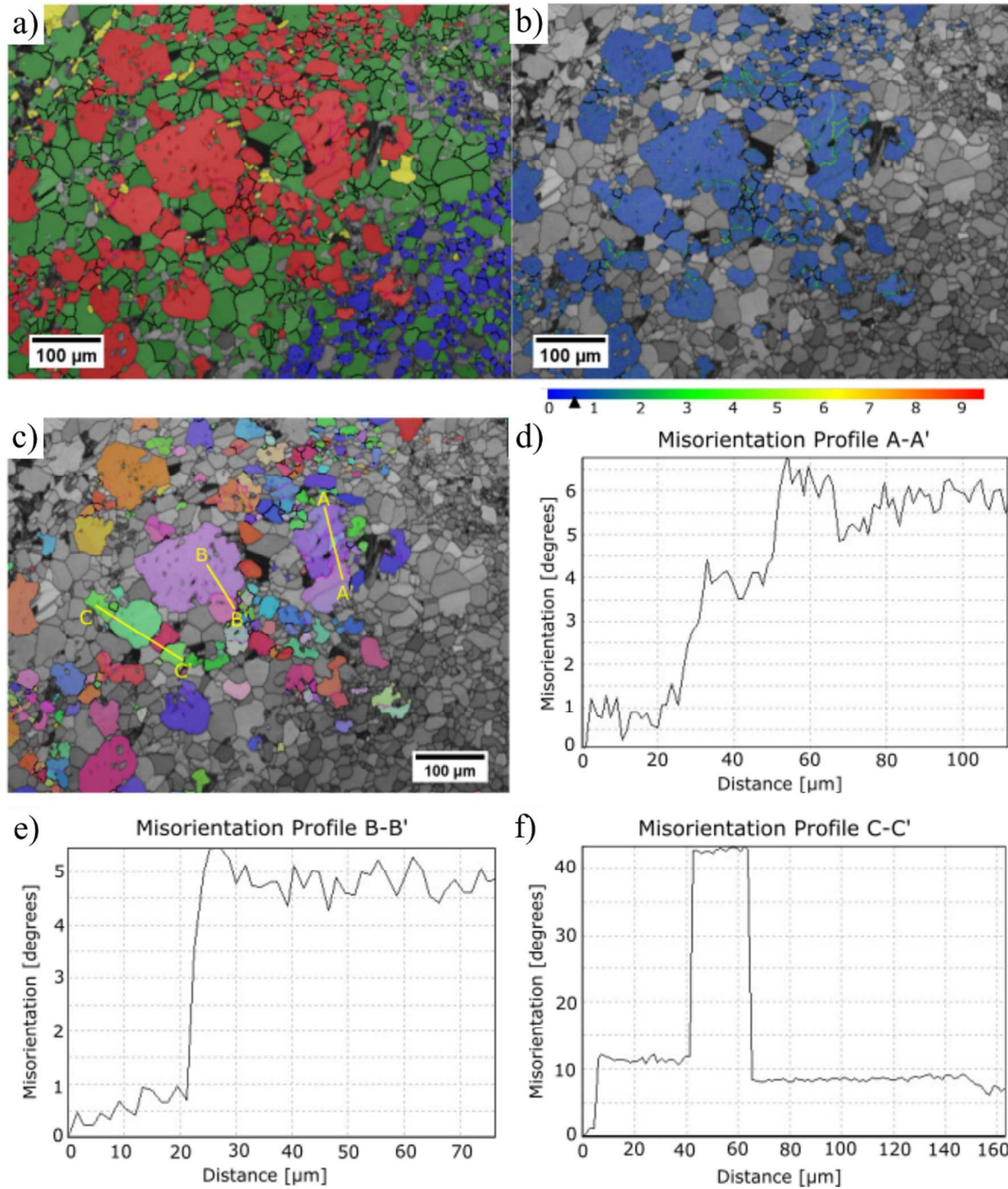


Figure S6 EBSD results of high strain domain (sample 0618). a) Phase map: Grt (red), Am (green), Opx (blue), Bt (yellow). b) Local Misorientation Map, and legend representing local misorientations from 0 (blue) to 9 degrees misorientation (red). The arrow indicates the average local internal misorientation. c) Inverse Pole Figure of garnet. Legend as in Fig. S3b. d) Misorientation profile A-A', location is shown in figure c). e) Misorientation profile B-B', location shown in figure d). f) Misorientation profile C-C', location shown in figure c).

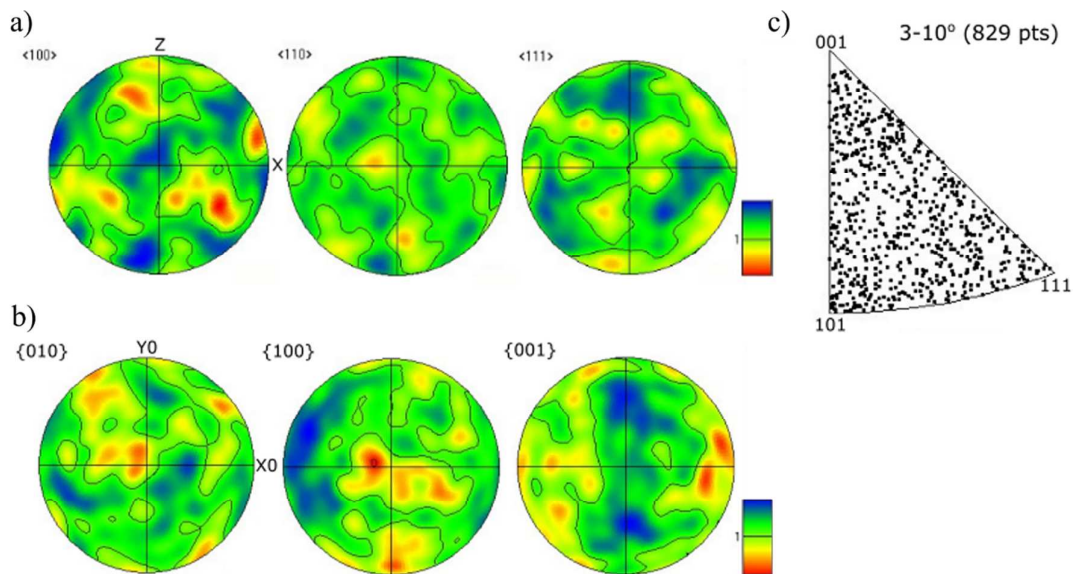


Figure S7 EBSD results of high strain domain (sample 0618). a) Pole figures of garnet. Equal area projections, upper hemisphere. Half width 15° , maximum intensity 1.96 and total number of grains is 223. The trace of the shear foliation is oriented NNE-SSW, pole figures are oriented with the trace of the mylonitic foliation parallel to the diameter (E-W). b) Pole figures of hornblende. Equal area projections, upper hemisphere. Half width is 15° , maximum intensity 2.04 and total number of grains is 856. c) Misorientation axis of low angle boundaries ($3\text{-}10^\circ$) in crystal coordinates.

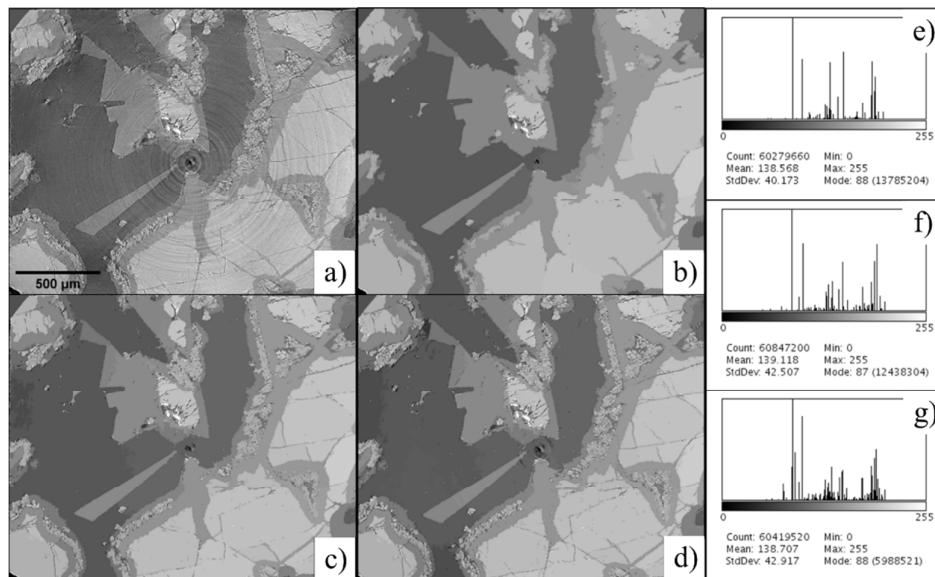


Figure S8 The image shows the results of Statistical Region Merging technique for increasing Q. Scale as in image a). a) Original data. b) SRM Q=2. c) SRM Q=10. d) SRM Q=25: note that the image is more detailed. e, f, g) Histograms relative to the three different

SRM parameters.

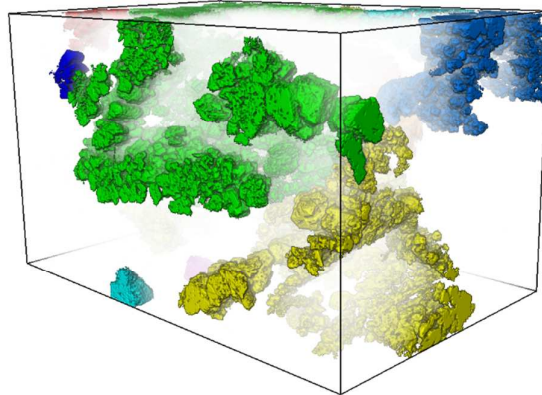


Figure S9 Label analysis of intermediate strain domain after erosion. The large interconnected voxel cluster is now divided in disconnected subvoxel clusters. Long side 2630 μm .

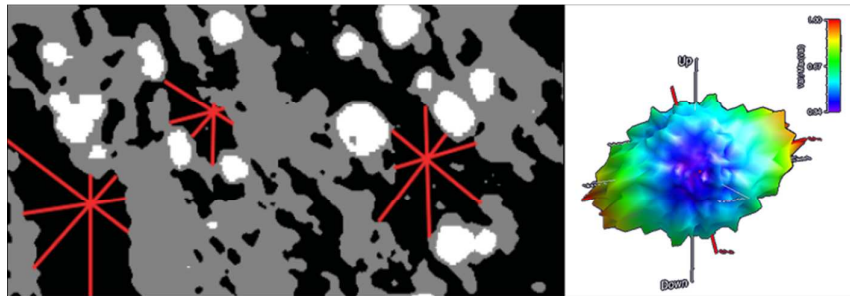


Figure S10 Quant3D explained. The tomographic data are first segmented to extrapolate the material of interest. Star points are placed within the segmented material: the distance of each star points to the next material boundary are calculated in many orientations and normalised. Simplified from Ketcham (2005).

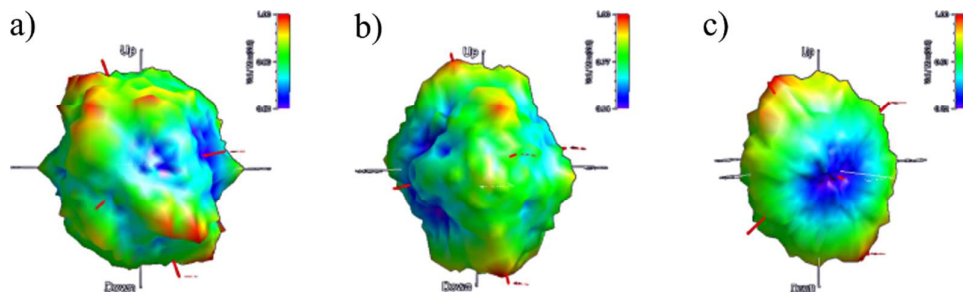


Figure S11 Results of Quant3D analysis on eroded data, from low strain (a) to high strain

(c). With increasing deformation, garnet grains evolve from isodiametric shapes to more progressively discoid shapes as a results of the deformation.

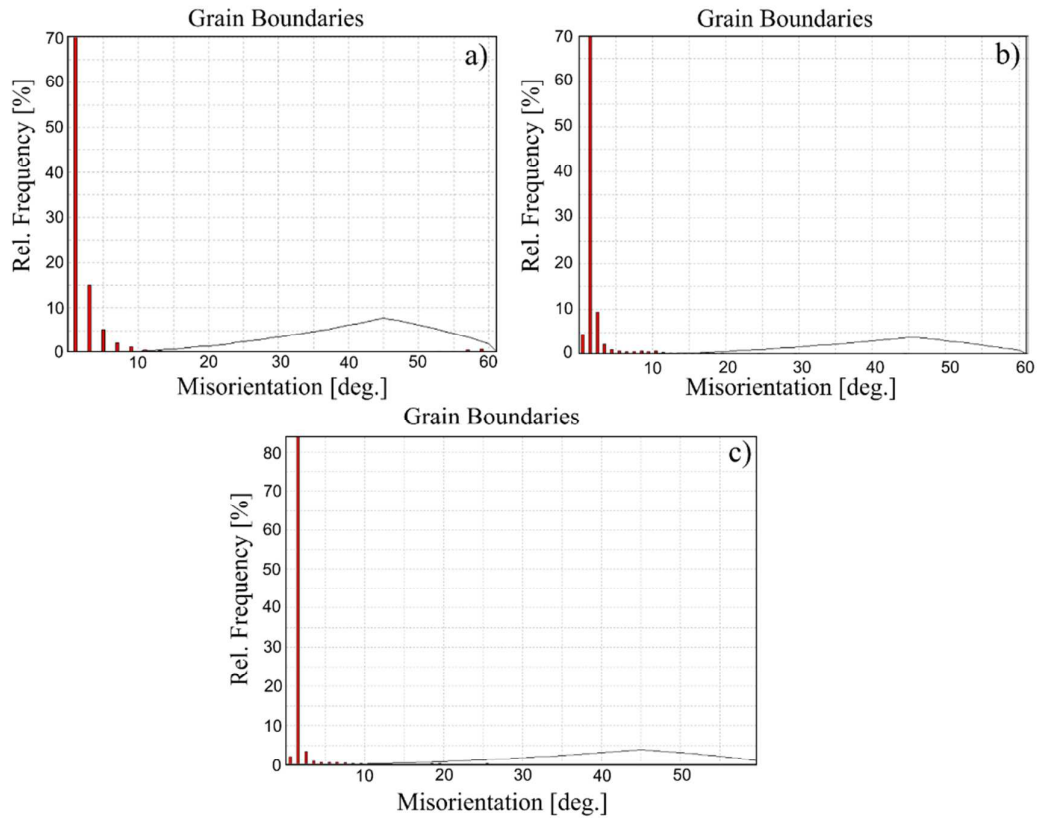


Figure S12 Histograms of GB cutoff misorientation (MO) angles: a) Low strain, b) Intermediate strain, c) High strain. The histograms confirmed that the vast majority of boundaries are indeed characterized by misorientation angles < 10 degrees- there has to be a sharp cutoff at 10 degrees, thus lending further support to the choice of using 10 degrees as threshold between low- and high-angle boundaries.

Sample	Na ₂ O	MgO	Al ₂ O ₃	FeO	CaO	SiO ₂	K ₂ O	TiO ₂	Cr ₂ O ₃	MnO	NiO	Total
#0618	0.009	6.853	21.605	28.263	5.709	38.981	0.004	0.039	0.004	0.705	0.000	102.171
#0618	0.036	6.405	21.874	28.018	5.360	39.270	0.003	0.097	-0.011	0.831	-0.011	101.873
#066B2	0.020	6.602	22.120	27.765	5.651	38.714	0.147	0.008	-0.003	1.157	0.015	102.196
#066B2	0.627	5.039	21.453	21.712	11.288	40.526	0.009	0.042	0.003	0.441	-0.008	101.131
#0617	-0.003	5.760	22.149	26.420	7.838	38.513	0.018	0.044	-0.009	0.865	-0.008	101.586
#0617	0.035	7.050	22.245	26.945	5.648	38.935	0.005	0.009	0.006	0.811	-0.010	101.679
#0617	0.044	5.801	22.150	25.930	8.612	38.965	0.006	0.051	-0.007	0.580	-0.009	102.122
#0617	0.021	5.868	22.291	25.077	9.592	38.815	0.000	0.065	-0.009	0.414	-0.013	102.120
#0617	0.030	6.173	22.366	24.130	9.262	38.685	0.001	0.043	0.004	0.971	0.005	101.668

Table S1 Electron microprobe chemical compositions of oxides in garnets, used to calculate the X-ray absorption coefficients.

	Low strain		Intermediate strain		High strain	
SiO ₂	38.86	39.17	38.33	38.06	38.9	38.56
TiO ₂	0	0.02	0	0	0	0
Al ₂ O ₃	21.77	21.1	21.09	21.54	21.22	21.05
Cr ₂ O ₃	0	0.01	0.01	0	0	0.03
Fe ₂ O ₃	0.53	0.23	0.42	1	0	0.07
FeO	24.9	24.33	25.2	23.21	26.04	26.73
MnO	1.15	1.17	0.58	0.6	0.56	0.59
MgO	5.79	6.64	6.03	6.66	7.74	7.08
CaO	7.87	7.42	7.26	7.67	4.58	4.81
Na ₂ O	0	0	0	0	0	0
K ₂ O	0	0	0	0	0	0
Totals	100.86	100.1	98.92	98.74	99.04	98.92
Oxygens	12	12	12	12	12	12
Si	2.996	3.03	3.011	2.977	3.031	3.024
Ti	0	0.001	0	0	0	0
Al	1.978	1.924	1.953	1.986	1.949	1.946
Cr	0	0.001	0.001	0	0	0.002
Fe ₃	0.03	0.013	0.025	0.059	0	0.004
Fe ₂	1.605	1.574	1.655	1.518	1.697	1.753
Mn	0.075	0.076	0.039	0.04	0.037	0.039
Mg	0.665	0.765	0.706	0.776	0.899	0.827
Ca	0.65	0.615	0.611	0.643	0.382	0.404
Na	0	0	0	0	0	0
K	0	0	0	0	0	0
Sum	8	8	8	8	7.995	8

Table S2 Representative garnet structural formulae for the low (#066B2) and high (#0618) strain domain obtained from the microprobe analyses at the University of Münster.

Bins [μm^3]	Low Strain	Cum. Freq.	Intermediate Strain	Cum. Freq.	High Strain	Cum. Freq.
2.00E+00	0		0		0	
4.00E+00	0		0		0	
8.00E+00	0		0		0	
1.60E+01	0		0		0	
3.20E+01	0		0		0	
6.40E+01	0		0		0	
1.28E+02	0		0		0	
2.56E+02	0		0		0	
5.12E+02	215	0.02%	2341	0.14%	0	0.00%
1.02E+03	209	0.05%	5868	0.64%	3244	0.18%
2.05E+03	152	0.09%	2208	1.01%	2502	0.43%
4.10E+03	122	0.17%	822	1.29%	1352	0.70%
8.19E+03	92	0.28%	348	1.54%	761	1.01%
1.64E+04	116	0.56%	174	1.78%	443	1.36%
3.28E+04	68	0.89%	97	2.04%	298	1.84%
6.55E+04	51	1.40%	62	2.40%	198	2.48%
1.31E+05	41	2.19%	42	2.85%	173	3.59%
2.62E+05	20	2.93%	33	3.59%	104	4.95%
5.24E+05	14	4.07%	26	4.74%	86	7.21%
1.05E+06	8	5.34%	14	6.03%	51	9.97%
2.10E+06	4	6.28%	17	9.24%	35	13.44%
4.19E+06	0	6.28%	8	11.80%	19	17.25%
8.39E+06	1	7.77%	3	13.94%	12	22.76%
1.68E+07	1	10.41%	4	19.72%	6	27.58%
3.36E+07	1	16.82%	0	19.72%	5	36.93%
6.71E+07	0	16.82%	0	19.72%	3	46.25%
1.34E+08	0	16.82%	0	19.72%	2	58.37%
2.68E+08	0	16.82%	0	19.72%	2	80.30%
5.37E+08	1	99.98%	0	19.72%	1	100.00%
1.07E+09	0	99.98%	1	100.00%	0	100.00%
Tot. Grt Vol.	4.81E+08		8.19E+08		1.43E+09	

Table S3 Frequency distribution data for non-eroded data. The first column of each dataset refers to absolute frequency, the second one to the cumulative frequency relative to the total amount of garnet in each sample.

Bins [μm^3]	Low Strain (eroded)	Cum. Freq.	Intermediate Strain (eroded)	Cum. Freq.	High Strain (eroded)	Cum. Freq.
2.00E+00	0		0		0	
4.00E+00	0		0		0	
8.00E+00	0		0		0	
1.60E+01	0		0		0	
3.20E+01	0		0		0	
6.40E+01	0		0		0	
1.28E+02	0		0		0	
2.56E+02	0		0		0	
5.12E+02	1101	0.14%	2428	0.15%	2379	0.08%
1.02E+03	638	0.30%	1215	0.15%	1628	0.18%
2.05E+03	390	0.49%	546	0.13%	1183	0.34%
4.10E+03	208	0.70%	297	0.15%	827	0.55%
8.19E+03	153	1.00%	153	0.15%	604	0.86%
1.64E+04	102	1.40%	80	0.16%	361	1.23%
3.28E+04	61	1.91%	71	0.29%	281	1.82%
6.55E+04	49	2.69%	56	0.44%	213	2.72%
1.31E+05	45	4.22%	39	0.63%	156	4.00%
2.62E+05	18	5.37%	30	0.96%	126	6.10%
5.24E+05	15	7.14%	23	1.39%	87	8.82%
1.05E+06	5	8.78%	22	2.81%	70	13.57%
2.10E+06	2	9.85%	18	4.46%	35	18.14%
4.19E+06	4	14.19%	7	3.28%	25	24.47%
8.39E+06	1	16.95%	5	5.27%	18	34.18%
1.68E+07	0	16.95%	2	3.43%	8	42.66%
3.36E+07	1	22.88%	0	0.00%	6	55.06%
6.71E+07	1	37.39%	1	6.32%	4	73.84%
1.34E+08	2	99.86%	1	14.54%	3	99.83%
2.68E+08	0	99.86%	0	0.00%	0	99.83%
5.37E+08	0	99.86%	1	54.73%	0	99.83%
1.07E+09	0	99.86%	0	0.00%	0	99.83%
Tot. Grt Vol.	2.89E+08		5.83E+08		1.13E+09	

Table S4 Frequency distribution data for eroded data. Bins refer to cubic micrometres. The first column of each dataset refers to absolute frequency, the second one to the cumulative frequency relative to the total amount of garnet in each sample.